

Master's Thesis
TVVR 09/5011

Near-field evolution and mixing of a negatively buoyant jet consisting of brine from a desalination plant

David Sánchez



Water Resources Engineering
Department of Building and Environmental Technology
Lund University

Department of Water Resources Engineering
TVVR 09/5011
ISSN 1101-9824

**Near-field evolution and mixing of a negatively
buoyant jet consisting of brine from a desalination
plant**

Lund 2009

Author: David Sánchez

Supervisor: Professor Magnus Larson

Examiner: Dr. Rolf Larsson

Copyright ©

Division of Water Resources Engineering
Department of Building and Environmental Technology
Lund University
P.O.Box 118, SE-221 00 Lund
<http://www.tvrl.lth.se/>

Printed in Sweden

Abstract

The aim of this study was to investigate the behavior of a dense jet discharged into lighter ambient water. This situation can be found for brine water discharged from desalination plants. Desalination plants discharge heavier brine water, generated in the process of manufacturing fresh water, to the receiving water, usually the sea.

Future extended use of desalination technologies implies larger quantities of saline water discharge to the environment. For that reason, it is of importance to study the mixing processes to avoid large concentration of salt, which may produce environmental problems.

The most efficient method to increase the dilution rate of the discharged water into the sea is by using a negatively buoyant jet. The design of this type of jet involves a wide range of variables. In this study a mathematical model was developed to simulate the jet behavior in order to determine the optimum discharge conditions for different scenarios.

The governing equations for a buoyant jet were employed in the model, including mass conservation for water and salt, and two momentum equations. In addition, several assumptions were introduced to simplify the model, for example, self similarity for the velocity and concentration profiles. The mathematical model was compared with data from previous experimental studies as well as from a new experiment performed within the present study.

In the model simulations performed in this study to reproduce the experimental runs it was difficult to observe a close relationship between the model and the experimental data for all experimental runs. For certain parameter ranges (*i.e.*, salinity, nozzle angle, nozzle diameter), model predictions were satisfactory. However, looking at different ranges in the densimetric Froude number there were always some runs that displayed larger discrepancies between the model simulations and the data obtained in the experiment.

A main conclusion of this study is that one or several of the assumptions used to derive the mathematical model is not satisfied in the experiment and some modifications of the equations derived are needed. Most likely a modified description of the entrainment coefficient is required that introduces a dependence on salinity and other parameters.

Acknowledgements

I would like to thank the Faculty of Engineering (LTH), Lund University, and particularly Water Resources Engineering (TVRL), where I have been studying for the last two years. I want to thank Magnus Larson, professor at TVRL, who has been the supervisor for this thesis, and Raed Alshaaer, doctoral student in the department and my mate for the experimental part. I am very grateful to both of them, because of their help during the course of this investigation.

Also, I would like to thank Center for Middle East Study (CMES) at Lund University because the project was partly funded by them, primarily the experimental work.

And finally I want to thank my family and my friends who were always close despite the distance.

Contents

Abstract.....	i
Acknowledgements	iii
List of tables	vi
List of Figures.....	vii
1. Introduction	1
1.1 Background.....	1
1.2 Objectives	3
1.3 Procedure	3
1.4 Desalination Technologies.....	3
1.4.1 History.....	3
1.4.2 Desalination methods	4
1.5 Desalination Discharges.....	7
2. Discharge of brine from desalination plants.....	9
2.1 Near field mixing	9
2.2 Far field mixing	10
2.3 Environmental impact.....	10
3. Near-field mixing of negatively buoyant jets	12
3.1 Previous studies	12
3.2 Jet trajectory.....	12
3.3 Mixing.....	13
4. Theoretical Model of jet evolution	14
4.1 Assumptions for the model	14
4.2 Mathematical model	14
4.2.1 Mass conservation.....	15
4.2.2 Momentum conservation.....	17
4.2.3 Solution of governing equations	19
4.2.4 Solving the governing equation.....	20
4.3 Sensitivity analysis	21
5. Non-dimensional analysis	25
5.1 Governing equations	25
5.2 Non-dimensional engineering properties.....	27
5.3 Non-dimensional engineering properties using realistic Froude numbers	29

6. Laboratory experiments	32
6.1 Setup	32
6.1.1 Water tanks.....	32
6.1.2 Flow meter and frequency meter.....	33
6.1.3 Pump.....	34
6.1.4 Hoses	34
6.1.5 Valves.....	34
6.1.6 Nozzles and nozzle support.....	35
6.1.6 Salt.....	36
6.1.7 Dye	36
6.2 Procedure	36
6.3 Observations	37
6.4 Data analysis	37
6.4.1 Reynolds number analysis.....	37
6.4.2 Densimetric Froude number analysis.....	40
7. Model comparison with data	43
7.1 Comparison between model simulations and experimental data.....	43
7.1.1 Jet trajectory comparison	43
7.1.2 Jet trajectory comparison for calibrated entrainment coefficient.....	45
7.2 Comparison between model simulations and data from Cipollina	49
8. Conclusions	50
References	51
Appendix	52

List of tables

Table 1 Froude number for real situations	29
Table 2 Correlation coefficient for x_m/D versus densimetric Froude number with salinity and initial nozzle angle fixed.....	40
Table 3 Correlation coefficient for x_m/D versus densimetric Froude number with salinity and nozzle diameter fixed.....	40
Table 4 Correlation coefficient for x_m/D versus densimetric Froude number with initial nozzle angle and diameter fixed	40
Table 5 Correlation coefficient y_m/D versus densimetric Froude number fixing salinity and initial nozzle angle	41
Table 6 Correlation coefficient y_m/D versus densimetric Froude number fixing salinity and nozzle diameter	41
Table 7 Correlation coefficient y_m/D versus densimetric Froude number fixing initial nozzle angle and diameter	42
Table 8 Data from the laboratory experiment, where θ is the initial nozzle angle, C is the concentration, D is the diameter, Q is the flow, and x_m and y_m coordinates for the maximum centerline height and location, respectively (see Figure 30).....	52
Table 9 Errors between experimental runs and the model simulation, calibrating the entrainment coefficient to obtain minimum difference.....	55

List of Figures

Figure 1 Water distribution in the world (ref: United States Geological Survey).....	1
Figure 2 Evolution of desalinated water production in the world (ref: IDA's Desalination Yearbook 2008-2009)	2
Figure 3 Evolution of desalinated water production in Spain (source: Torres Corral, 2004).....	2
Figure 4 Desalination methods distribution for newly contracted plants (Ref: IDA's Desalination Yearbook 2008-2009)	4
Figure 5 Desalination methods distribution for the largest producers (ref: IDA's Desalination Yearbook 2008-2009)	5
Figure 6 Top 25 Petroleum producers in the world (Ref: US Energy Information Administration).....	5
Figure 7 Shoreline discharge of brine (Bleninger <i>et al.</i> , 2008).....	8
Figure 8 Submerged discharge via pipeline with a nozzle creating a negatively buoyant jet (Bleninger <i>et al.</i> , 2008).....	8
Figure 9 Near and far field regions (Ruiz Mateo <i>et al.</i> , 2008)	9
Figure 10 Posidonia meadows habitat (Ruiz Mateo <i>et al.</i> , 2008).....	11
Figure 11 Trajectories for a negatively buoyant jet.....	13
Figure 12 Definition sketch for a circular buoyant jet (Jönsson, L. (2004)).....	16
Figure 13 Definition sketch for determining the buoyancy force on a circular jet	19
Figure 14 Definition sketch of geometric quantities for the jet.....	20
Figure 15 The effect of calculation step size Δs on the jet trajectory	21
Figure 16 The effect of entrainment coefficient on the jet trajectory.....	22
Figure 17 The effect of initial velocity on the jet trajectory.....	23
Figure 18 The effect of initial concentration on the jet trajectory.....	23
Figure 19 The effect of nozzle angle (initial direction of discharge) on the jet trajectory	24
Figure 20 Horizontal location of maximum jet rise height as a function of densimetric Froude number for different initial nozzle angles	28
Figure 21 Maximum jet rise height as a function of densimetric Froude number for different initial nozzle angles	28
Figure 22 Maximum dilution rate as a function of densimetric Froude number for different initial nozzle angles	29
Figure 23 Horizontal location of maximum jet rise height as a function of densimetric Froude number for different initial nozzle angles for a lower Froude number range	30
Figure 24 Maximum jet rise height as a function of densimetric Froude number for different initial nozzle angles for a lower Froude number range	31
Figure 25 Maximum dilution rate as a function of densimetric Froude number for different initial nozzle angles for a lower Froude number range	31
Figure 26 Water tanks used in the experiment on negatively buoyant jets	33
Figure 27 Flow meter and tanks for saline water used in the experiment.....	34
Figure 28 Valves utilized for flow control and air evacuation	35
Figure 29 Nozzle support system on which the nozzle was attached.....	36
Figure 30 Jet measured parameters	37

Figure 31 Non-dimensional distance to the location of the maximum height of jet centerline (x_m/D) versus the Reynolds number for the range $2500 < Re_y < 5000$	38
Figure 32 Non-dimensional distance to the location of the maximum height of jet centerline (x_m/D) versus the Reynolds number for the $Re_y > 5000$	38
Figure 33 Maximum height of jet centerline (y_m/D) versus Reynolds number ($2500 < Re_y < 5000$).....	39
Figure 34 Maximum height of jet centerline (y_m/D) versus Reynolds number ($Re_y > 5000$).....	39
Figure 35 Non-dimensional distance to the location of the maximum height of jet centerline (x_m/D) versus densimetric Froude number ($D = 0.0033$ m).....	41
Figure 36 Distribution of simulation errors	44
Figure 37 Simulation error versus Froude number.....	45
Figure 38 Simulation versus Reynolds number.....	45
Figure 39 Distribution of simulation errors when the entrainment coefficient value was calibrated	46
Figure 40 Distribution of the entrainment coefficient when it was calibrated against data	47
Figure 41 Distribution of the entrainment coefficient when it was calibrated against data differentiated with respect to salinity employed during the experimental run	47
Figure 42 The entrainment coefficient when it was calibrated against data versus the densimetric Froude number	48
Figure 43 The entrainment coefficient when it was calibrated against data versus the densimetric Froude number for a sub-set of the data	49
Figure 44 Distribution of simulation errors for the Cipollina <i>et al.</i> data.....	49

1. Introduction

The future increase of sea water as a source for producing fresh water will affect the environment close to the desalination plants because of the discharge of very saline water to the sea. It will be a significant problem for the ecological habitat if a desalination plant generates a large discharge since an increase in the salinity in the vicinity of the discharge point is expected.

1.1 Background

The increase of the world's population has resulted in a parallel increase in the demand for fresh water for drinking, requirements for extra food production, and for industrial uses. Some countries have large problems to obtain sufficient fresh water and as a result they have looked into new sources for supplying water.

Water covers approximately 75% of the earth's surface; however, only 3% is fresh water. Furthermore, only 0.3% of the fresh water is surface water such as rivers, swamps, or lakes. Groundwater constitutes around 30% of the total fresh water and ice caps and glaciers contain almost 69% of all the fresh water. (United States Geological Survey)

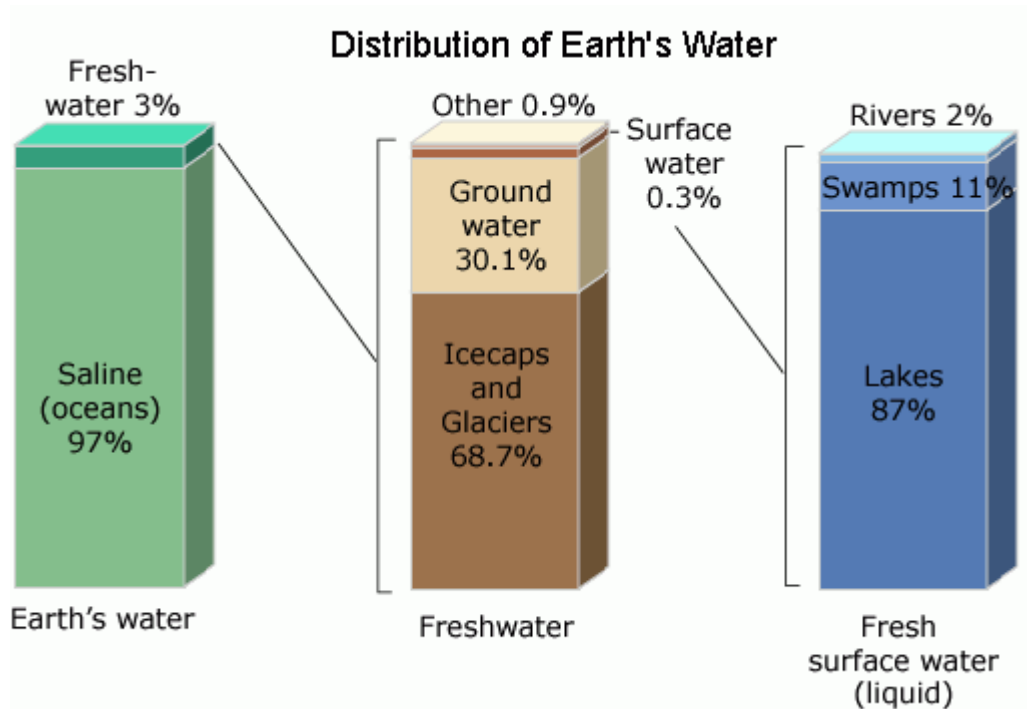


Figure 1 Water distribution in the world (ref: United States Geological Survey)

Traditional water sources (lakes, rivers, dams, artesian wells) have not been enough to cover all the demand in some countries so they started to look for other sources. The attention turned to saline water as a possible new source for fresh water, as it includes a known technique. Desalination techniques have been used for a long time to remove salt from sea water, making it viable as drinkable water. At first, the techniques were very expensive to

utilize, however, after developing and improving the techniques they have become more economical and competitive.

Figure 2 shows how the production of desalinated water has increased every year. The average increase is 19.2% per year, but in last 10 years the average increase has been 7.9%.

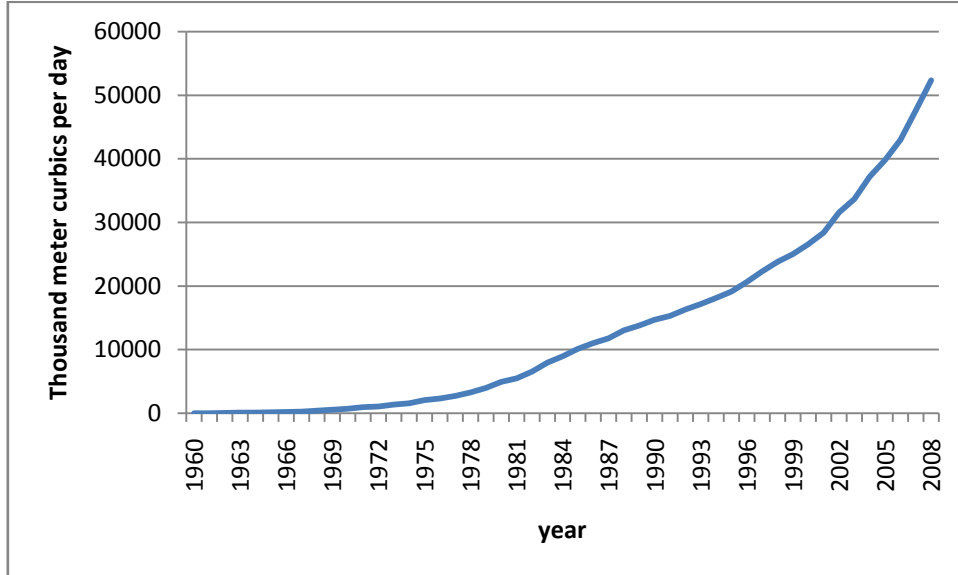


Figure 2 Evolution of desalinated water production in the world (ref: IDA's Desalination Yearbook 2008-2009)

Spain is one of the largest producers of desalinated water in the world and it is also one of the driest countries in Europe. Due to this fact it needs to desalinate large amounts of saline water to have sufficient supply for drinking, irrigation, and industrial applications. During the last 20 years a large increase in the desalinated water production has been observed due to several periods of serious water shortage (see Figure 3).

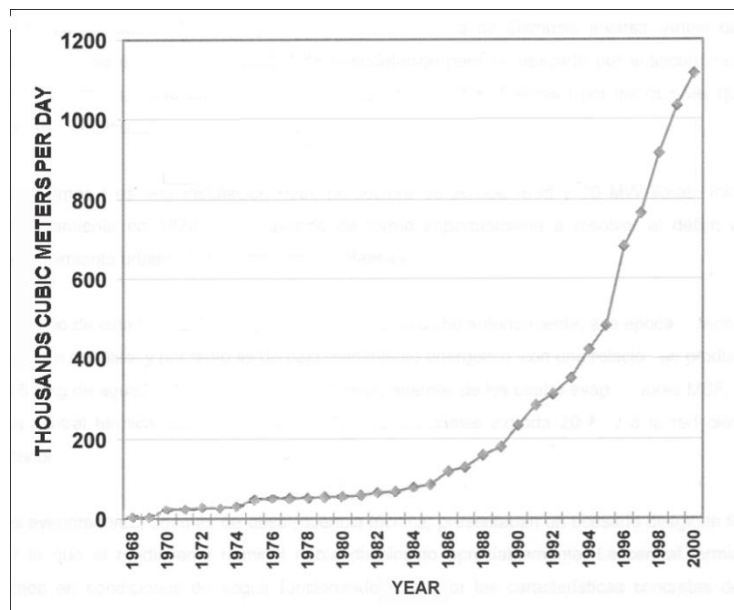


Figure 3 Evolution of desalinated water production in Spain (source: Torres Corral, 2004)

1.2 Objectives

The main objectives of this thesis are to investigate how a negatively buoyant jet consisting of brine from a desalination plant develops in the near field and how the jet is mixed with the ambient water. Increased understanding of the performance of negatively buoyant jets will allow for less expensive and more efficient systems to discharge brine from desalination plants, as well as higher dilution rates and improved environmental conditions in the vicinity of the discharge point.

The detailed objectives may be summarized:

- to develop a mathematical model based on the fundamental governing equations for a buoyant jet discharged into a quiescent ambient
- to perform a laboratory experiment on the evolution of negatively buoyant jets
- to employ the laboratory data for model calibration and validation
- to utilize the validated model for optimization of discharge systems and for evaluation of different discharge scenarios

1.3 Procedure

A general survey of the literature was made regarding near-field properties of negatively buoyant jets with focus on brine discharge from desalination plants. Data on jet evolution and mixing properties were compiled from the literature. In addition, an experiment was performed at the Water Resources Engineering (TVRL) laboratory at a reduced scale that still ensured turbulent jet behavior. A mathematical model of the jet evolution was developed based on the mass and momentum conservation equations. The model was calibrated and validated towards the compiled data base and the additional data collected in the experiment. After model development different scenarios were evaluated to investigate model sensitivity towards different parameters and to determine discharge conditions that achieve optimal mixing in the near field.

1.4 Desalination Technologies

1.4.1 History

The idea of separating salt from the water is very old. In the beginning the main idea was to obtain the salt from sea water because it was a precious commodity. Some years later, at the end of 17th century, people started to investigate how to produce fresh water in remote locations and, especially, on naval ships at sea. The first desalination plant was built on the island of Curaçao in the Netherlands Antilles in the year 1928 (Gleick, 2000).

During the last years desalination water technologies have been investigated and improved to increase the fresh-water capacity per plant and to decrease desalinated fresh-water prices.

1.4.2 Desalination methods

There are several methods for water desalination; however, the methods are typically divided into two general groups. The first one is through the use of thermal heat processes and the second one utilizes membrane and filtration processes. Employing thermal heat processes it is possible to have water with much lower salt content (25 ppm) than the technique incorporating membrane and filtration processes (500 ppm). However, membrane and filtration processes normally uses less energy and produces water that meets drinking water standards in quality (Gleick, 2000).

Figure 4 shows new contracted desalination capacities in the world. It can be seen that filter processes are becoming more common in recent years compared to thermal processes due to the increase in the fuel price.

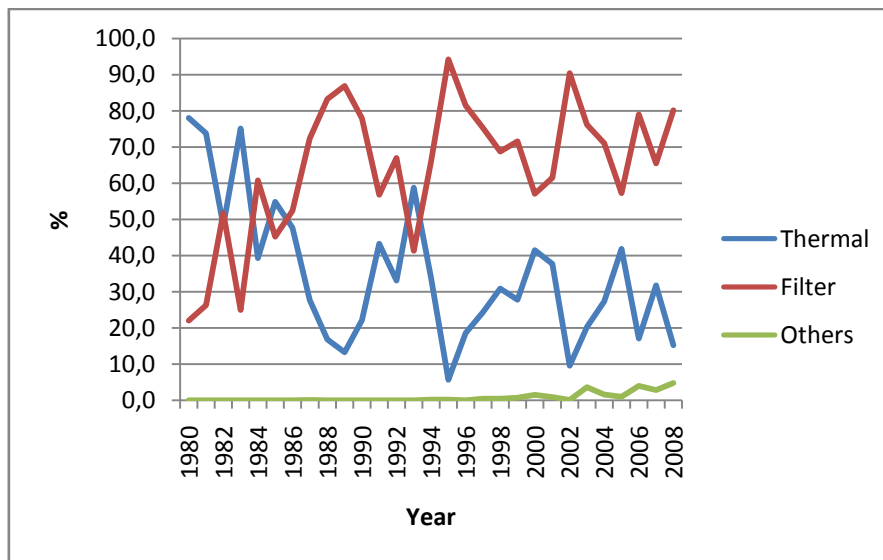


Figure 4 Desalination methods distribution for newly contracted plants (Ref: IDA's Desalination Yearbook 2008-2009)

1.4.2.1 Thermal processes

Thermal processes are normally used in countries with no shortage in the energy supply, such as those situated in the Persian Gulf because of their easy access to petroleum. As observed in Figure 5, Saudi Arabia, United Arab Emirates, Kuwait, Qatar, Libya, Oman, and Bahrain use thermal processes. They are in the top 20 among petroleum producers as shown in Figure 6.

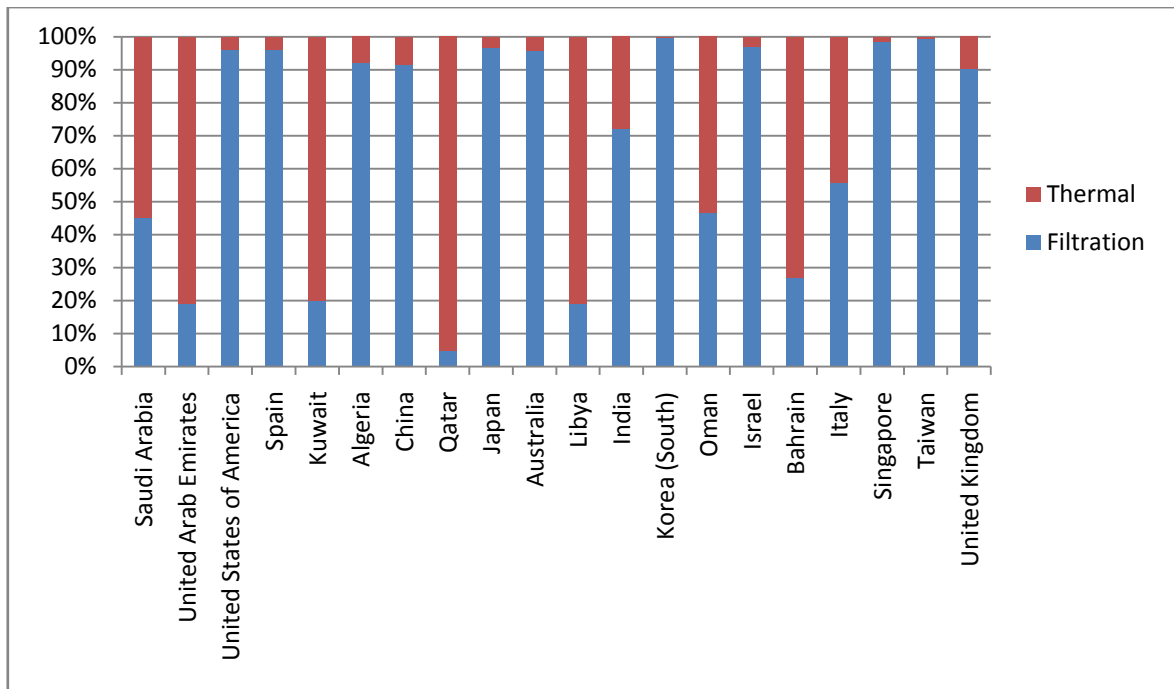


Figure 5 Desalination methods distribution for the largest producers (ref: IDA’s Desalination Yearbook 2008-2009)

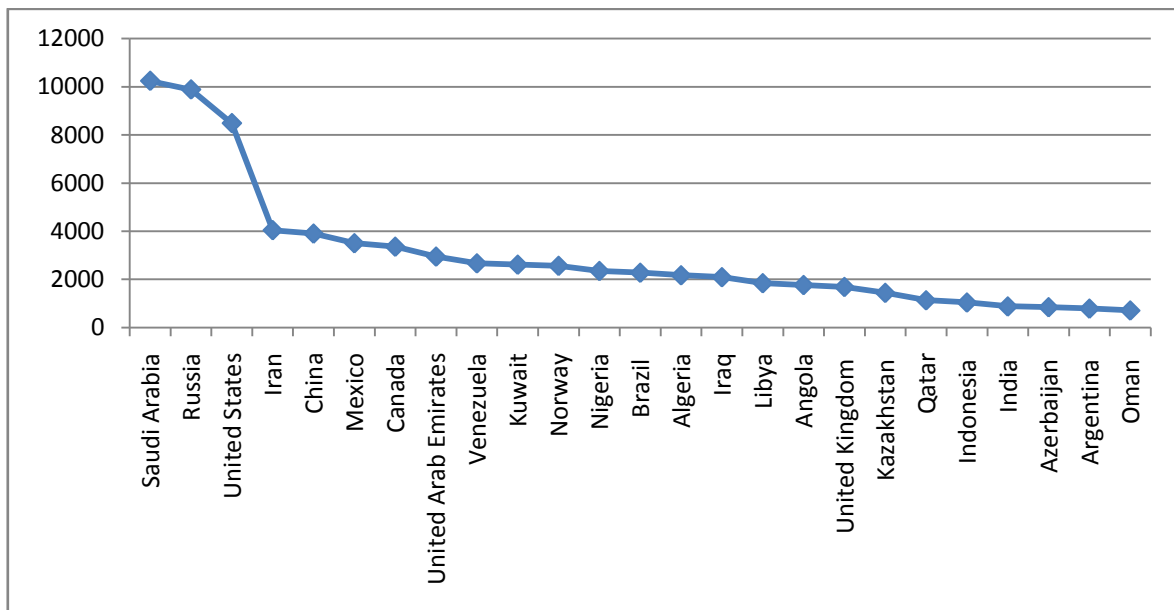


Figure 6 Top 25 Petroleum producers in the world (Ref: US Energy Information Administration)

The idea behind thermal processes is based on generating evaporation. The approach is to produce water vapor in order to separate the fresh water from the salts and then condensate it to obtain the fresh water. Modification of the pressure can be employed to reduce the boiling point in order to speed up the process. These processes have a problem with scaling. Carbonates and sulfates found in sea water can precipitate out of solution and cause thermal and mechanical problems.

The thermal processes need a lot of energy compared with the membrane and filtration processes, but normally thermal processes desalination factories are situated close to the power plants to use the residual energy from these to heat sea water and reduce the requirements of energy. Sometimes, it is difficult to use a combined cycle because it needs a large area to provide space for the power plant and the desalination plant.

1.4.2.1.1 Multi-Stage Flash Distillation

This is a widely used thermal method. In this method, evaporation flashing occurs from the bulk liquid (not on a heat-exchange surface). This technology reduces the factory size.

Firstly, the sea water is heated in a container. This is usually attained by condensing steam on a bank of tubes carrying sea water through the brine heater. Heated water is passed to another container where the surrounding pressure is lower than in the previous one. It is the sudden introduction of this water into a lower pressure container that causes it to boil so rapidly. Typically only a small percentage of this water is converted into steam. Consequently, it is normal that the remaining water will be sent through a series of additional stages, each possessing a lower ambient pressure than the previous. As steam is generated, it is condensed on tubes of heat exchangers that run through each stage. (Gleick, 2000)

1.4.2.1.2 Multiple-effect Distillation

In this method, evaporation occurs in different tanks with varying pressure in each; the normal succeeding step would be to add thermal energy, however it is not needed since the reaction will be driven by the different degrees of pressure.

Steam is condensed in a condenser. Saline water is used in the condenser to cool steam. This saline water becomes warm due to the energy transfer in the condenser and the steam becomes distilled water. Saline water is distilled and it is introduced into a container saving energy. It is not possible to distill all the saline warm water which was used in the condenser because the amount of water needed to condense is larger than the amount of water possible to distill. (Gleick, 2000)

1.4.2.2 Membrane and Filtration Processes

Membrane and filtration processes are used to desalinate more than half of the total amount of water. These processes can remove microorganisms and many organic contaminants. The two more important processes are electrodialysis and reverse osmosis. Membrane technology is being used more readily today due to technological advancements and subsequent decreases in price.

1.4.2.2.1 Electrodialysis

This process utilizes electrochemical separation in order to prevent passing salt ions through a membrane. Fresh water passes through the membrane, but salts cannot pass. This process can

treat water which has more suspended solids than reverse osmosis so it needs less pre-chemical filtration. Normally we can use some chemical products to try to bind the particles together into a flocculent in order to more easily filter them due to their increased size.

1.4.2.2.2 Reverse osmosis

This method uses pressure to move water through a semi-permeable membrane where the salts will be retained. The amount of energy depends on the salt concentration and the external water temperature. The quantity of desalinated water which can be obtained ranges between 30% and 85% of the volume of the input (Gleick, 2000).

The new technologies are trying to decrease prices with new membranes which retain more salts and are suitable to use more times.

1.4.2.3 Other Desalination Processes

There are other methods to desalinate sea water; however, they are used less frequently than the other techniques mentioned above (less than 1% of the time). There are three major methods: Ion Exchange, Freezing and Membrane Distillation.

Ion Exchange uses resins to remove undesirable ions in the sea water. This method is normally employed to remove calcium and magnesium in municipal water treatment plants.

The Freezing method exploits the fact that salts are insoluble in ice. This process has some advantages such as less required energy for operation, lower corrosion in the entire system, and little scaling or precipitation. However, it is not a common method for desalinating water but it is sometimes used in the treatment of industrial waste water.

Membrane Distillation combines thermal distillation and membranes. First, it uses thermal processes and then the vapor is passed through some membranes. Finally this vapor is condensed as fresh water. It is very simple and it needs only small temperature differences, but it is not often used because it requires more space and more pumping energy (Gleick, 2000).

1.5 Desalination Discharges

In early applications, the discharge from desalination plants occurred directly to the bottom of the sea (Figure 7). This system was not satisfactory because the mixing between the ambient sea water and the saline water from the discharge was very poor and the salt concentration was locally very high. Discharged water, which has higher density is trapped along the bottom and does not mix easily with sea water, creating horizontal stratification due to the salinity difference. The dilution rate was very small and large concentrations of salt could be found creating detrimental effects for the environment.

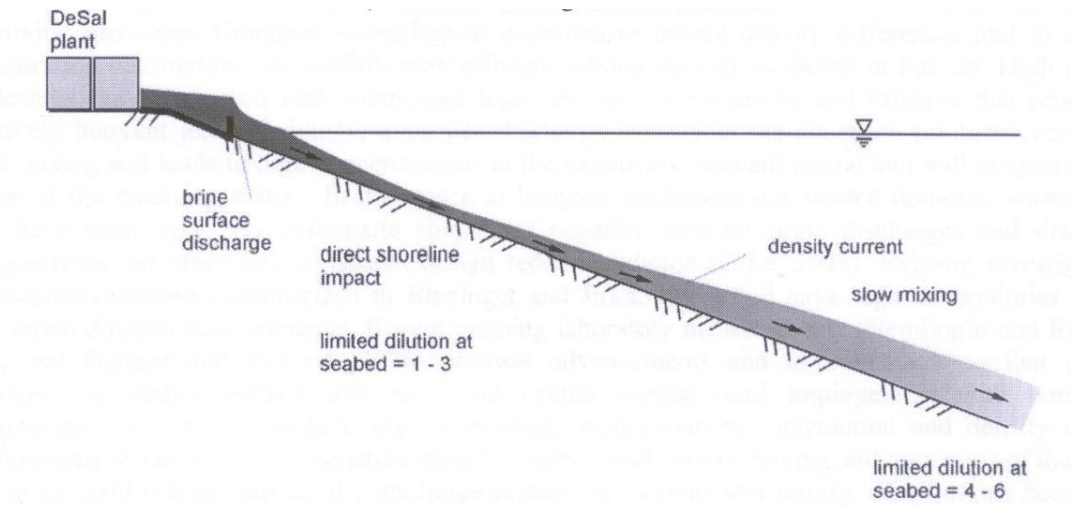


Figure 7 Shoreline discharge of brine (Bleninger *et al.*, 2008)

Nowadays, the saline water is often discharged using nozzles at the bottom of the sea Figure 8). The nozzles have a specific positive angle with regard to the sea bed to improve the mixing. Using such a positive angle jet, it is possible to create a long travel for the brine jet before it reaches the bed, and therefore there is an increase in the mixing and a larger dilution.

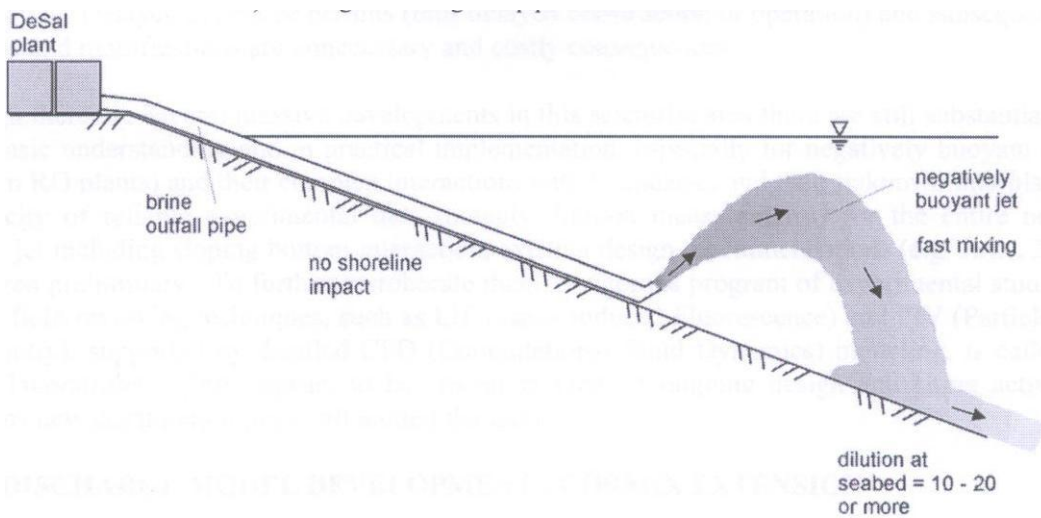


Figure 8 Submerged discharge via pipeline with a nozzle creating a negatively buoyant jet (Bleninger *et al.*, 2008)

2. Discharge of brine from desalination plants

It is possible to identify two different regions for the mixing of a brine jet with an ambient: the near and far field. The near-field region is primarily characterized by the initial momentum flux, buoyancy flux, and outfall geometry. These three parameters affect the mixing in this region. The second region, known as the far field, encompasses the area after which the brine has traveled some distance away from the nozzle, where the source characteristics are less important. Thus, in the far field the important characteristics are the conditions prevailing in the ambient.

Figure 9 illustrates the difference between the near and the far field depending on how the effluent from the desalination plant was discharged (directly to the bottom or discharging a negatively buoyant jet through a nozzle).

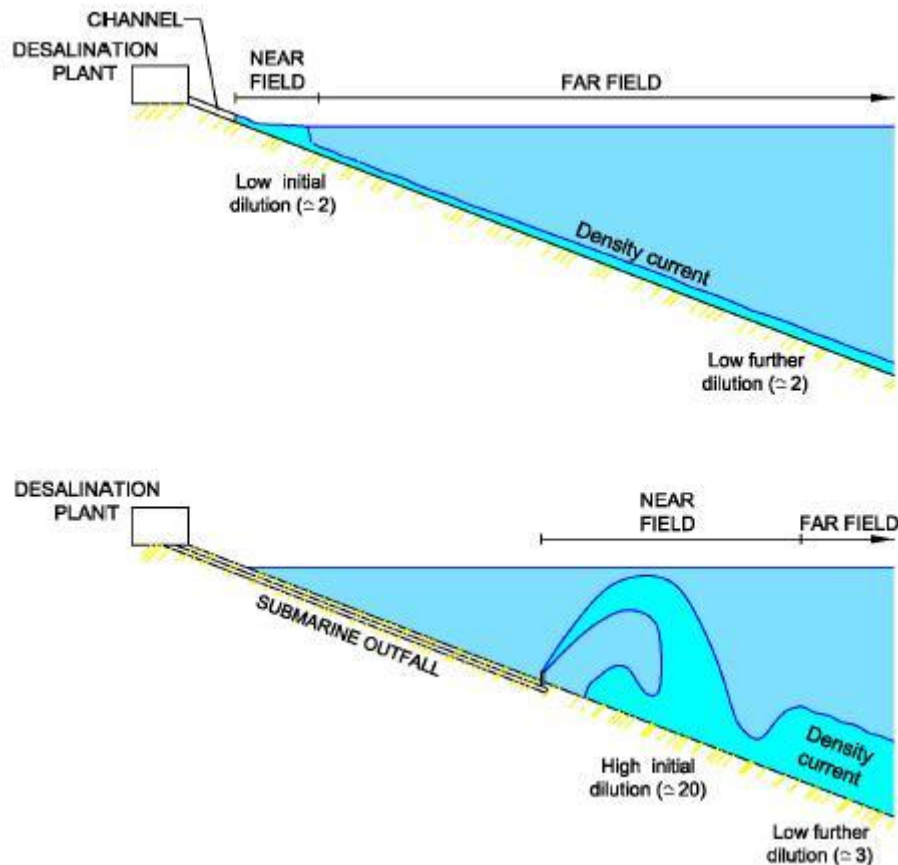


Figure 9 Near and far field regions (Ruiz Mateo *et al.*, 2008)

2.1 Near field mixing

Near-field mixing is the part which is studied in this investigation. As discussed above, near-field mixing depends primarily on the source characteristics.

The positive discharge angle (defined as being counter-clockwise from the bed) of the nozzle causes a longer mixing area where saline water can be more diluted. The dilution rate in this

area is large because of the turbulence causing entrainment and diffusion. In general, if the trajectory is longer, the dilution rate becomes larger.

In order to increase the trajectory length, it is favorable to increase the initial momentum by increasing the jet velocity. So, as the velocity becomes larger, the trajectory becomes longer. But increasing the initial velocity implies a larger cost due to the requirement of a larger energy input. Thus, it may be necessary to study a large number of cases to find an optimum solution as a balance between the required costs and the obtained dilution rate.

2.2 Far field mixing

After the near field mixing, the dilution rate is controlled by the far field mixing, which does not exhibit a strong dependence on the initial momentum flux, buoyancy flux and outfall geometry. In the far-field mixing an important parameter is the magnitude of the sea current. The rate of mixing in this region is normally much smaller than in the near field due to the small velocity of the sea current that transports and mixes the brine. Outside the surf zone, the velocity is in many cases less than 5 cm/s (around 0.1 km/hr). However, the current speed and direction could be highly variable.

2.3 Environmental impact

High salinity may have a significant impact on marine life and the ecological habitat. Because of this fact, it is very important to obtain rapid mixing between saline water discharged from the desalination plants and the sea water in order to achieve a large dilution rate.

Figure 10 shows how an outfall from a desalination plant affects Posidonia meadows. The desalination plant is situated in Mazarron, in the south of Spain. In this case, the salt concentration in the sea was 37.5 psu, the effluent (brine) concentration was 68.2 psu, and the flow was 1.65 m³/s. The figure illustrates that there are not any Posidonia meadows close to the outfall (Ruiz Mateo *et al.*, 2008).

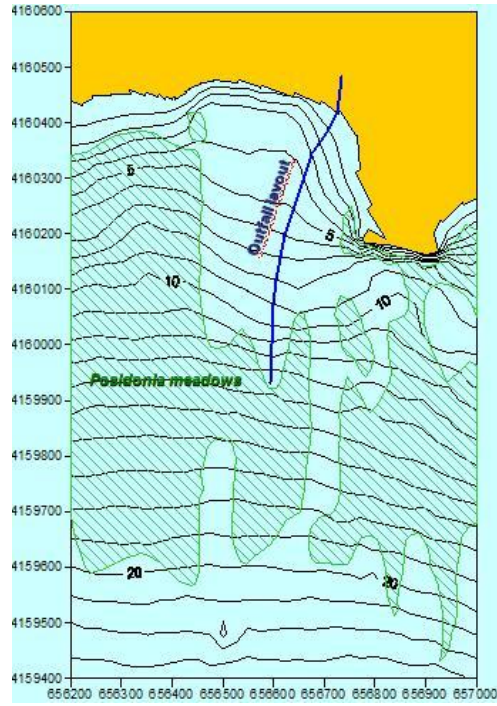


Figure 10 Posidonia meadows habitat (Ruiz Mateo *et al.*, 2008)

3. Near-field mixing of negatively buoyant jets

As pointed out above, a good mixing is important to avoid biological problems in the vicinity of the discharge and for that reason negatively buoyant jets are used because they have a larger mixing and a better dilution rate than direct discharge to the bottom.

The most important part of the mixing occurs in the near field where the mixing depends on the initial parameter values at the nozzle, such as the momentum, nozzle angle, and diameter of the nozzle. The far field mixing depends typically on the large-scale sea currents.

3.1 Previous studies

One of the first studies concerning dense jets involved in negatively buoyant flow was carried out by Zeitoun *et al.* (1972), where a part of the investigation focused on dilution measurements at the maximum rise level of the jet trajectory. Initial jet angles of 30°, 45°, and 60° were studied and 60° was determined to be the best for the dilution rate.

Later, several studies, for example, Roberts (1997) and Pincince and List (1973), focused on the 60-degree case and obtained jet trajectories and mixing data for this angle.

Cipollina *et al.* (2005) investigated different nozzle angle configurations. The study included the angles 30°, 45°, and 60°, and the jet trajectory was determined in those experiments. However, the dilution rates were not included in the investigation.

Bleninger and Jirka (2007) developed a software called Cormix to calculate jet trajectories and dilutions rates. Based on simulation results, they suggested a nozzle angle between 60° and 75° for a flat bottom to obtain the maximum dilution rate. Furthermore, they suggested an angle between 45° and 60° for moderate bottom slopes (between 10° and 20°) and an angle between 30° and 45° for strong slopes (30°).

Data from the studies by Cipollina *et al.* (2005) were used in this investigation to compare with the mathematical model that was developed.

3.2 Jet trajectory

The optimum trajectory is the one that achieves the best dilution rate. In the case where the density of the jet water is larger than the density of the ambient water, the trajectory will be formed by a negatively buoyant jet. The jet starts from the bottom, with a positive angle; therefore the jet has a trajectory that initially points towards the sea surface. However, because of the buoyancy force the jet changes its orientation until it has a trajectory that points towards the bottom. Eventually, the jet impacts the bottom and from that point the far-field mixing starts (Figure 11 Trajectories for a negatively buoyant jet).

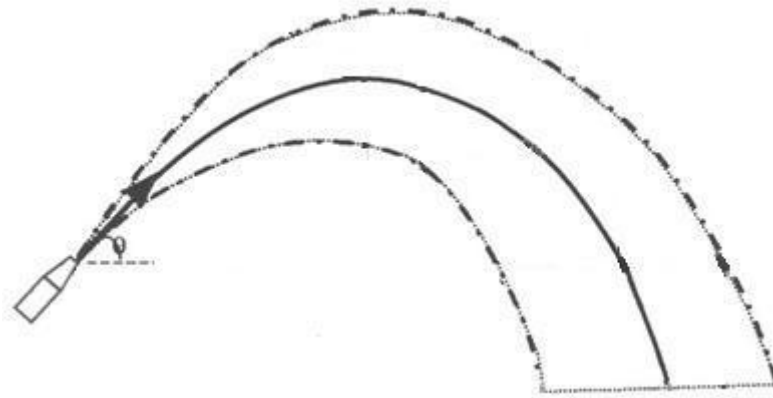


Figure 11 Trajectories for a negatively buoyant jet

3.3 Mixing

The jet mixing is due to the ambient water that is entrained into the jet. The higher velocity the jet has, the larger the entrainment and resulting mixing. However, to increase the initial velocity of the jet typically implies increased pumping costs since a higher velocity requires the supply of more energy. Thus, it is necessary to look for an efficient way to find an optimum dilution rate.

4. Theoretical Model of jet evolution

To develop a mathematical model of a negatively buoyant jet discharged into an ambient there are several equations which need to be formulated. These equations include the continuity equations for water and for the tracer (*i.e.*, salt) as well as the momentum equations in the x and z directions (see Figure 12).

After the model has been developed it is necessary to check its performance through comparison with data and to carry out a comprehensive sensitivity analysis with regard to the main model parameters. Such an analysis will make it possible to observe if there is anything incorrect concerning the model results.

4.1 Assumptions for the model

In order to arrive at a reasonably simple model, it is necessary to make certain assumptions in the model development. The main assumptions made here are (Jönsson, L. (2004)):

- Hydrostatic pressure distribution in the ambient water and in the jet.
- Variations in the density within the jet are small compared to the receiving water density.
- Density differences are too small to affect inertia forces, but are important for the buoyancy force (the Boussinesque approximation). This assumption implies that the continuity equation can be described in terms of volumes instead of mass.
- The horizontal momentum of the jet is constant along the jet trajectory.
- The jet is symmetrical in a plane perpendicular to the jet axis.
- There is similarity for velocities and concentrations (or density deficit) in planes perpendicular to the jet axis (Gaussians distributions).
- There is no influence from the boundaries of the receiving water.
- There is a linear relationship between concentration and density.

4.2 Mathematical model

It was assumed that the velocity profile and the salt concentration in the jet for the model are following Gaussian distributions:

$$u = u_m \cdot e^{-\left(\frac{r}{r_u}\right)^2} \quad (1)$$

$$c = c_m \cdot e^{-\left(\frac{r}{r_c}\right)^2} \quad (2)$$

Where:

r is the transverse or radial distance from the jet axis

u is the velocity at r

u_m is the maximum velocity in the jet (this velocity occurs at the jet centerline)

r_u is the characteristic jet width for velocity

c is the concentration at r

c_m is the maximum concentration which can be found at the centerline.

r_c is the characteristic jet width for concentration

These typical values for jets are assumed as well:

$$\frac{r_u}{x} = 0.107 \pm 0.003 \quad (3)$$

$$\frac{r_c}{x} = 0.127 \pm 0.004 \quad (4)$$

$$\lambda = \frac{r_c}{r_u} = 1.2 \quad (5)$$

Also, a linear relationship between density and concentration is employed:

$$\rho = \rho_a + k \cdot c \quad (6)$$

Where:

ρ is the jet density

ρ_a is the ambient density

k is a constant

c is the salt concentration

4.2.1 Mass conservation

In this section, the conservation of mass (continuity equation) is developed for the water and for the tracer (salt).

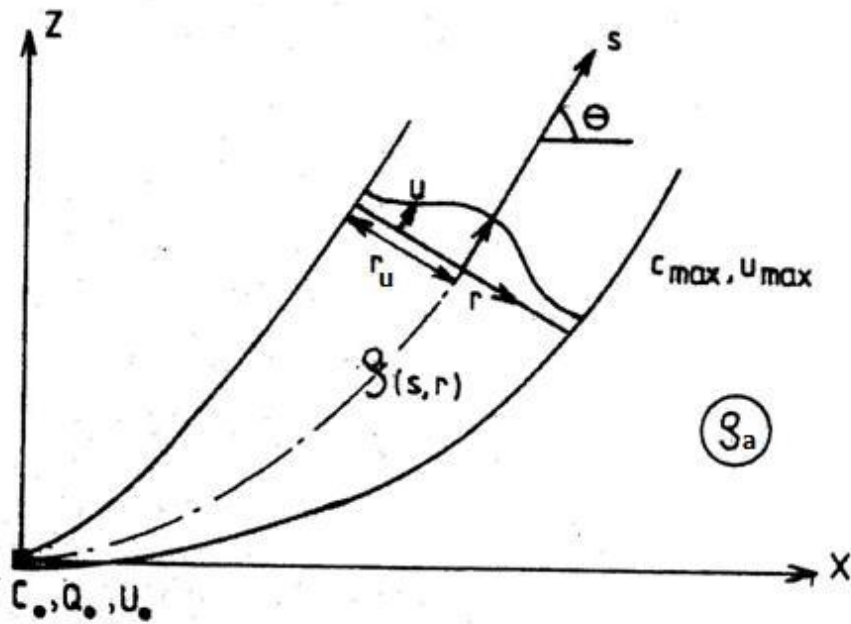


Figure 12 Definition sketch for a circular buoyant jet (Jönsson, L. (2004))

The continuity equation for the water describes how ambient water is entering into the buoyant jet, increasing its size because it is assumed that the water is not compressible:

$$\frac{dQ}{ds} = \alpha \cdot u_m \cdot 2\pi \cdot r_u \quad (7)$$

Where:

Q is the flow in the jet

s is the coordinate following the jet axis

α is the entrainment coefficient

and other variables are as defined above.

A development of equation (7) is carried out according to:

$$\begin{aligned} Q &= \int_0^\infty u \cdot 2\pi \cdot r \cdot dr = \int_0^\infty u_m \cdot e^{-\left(\frac{r}{r_u}\right)^2} \cdot 2\pi \cdot r \cdot dr = 2\pi \cdot u_m \int_0^\infty r \cdot e^{-\left(\frac{r}{r_u}\right)^2} dr = \\ &= 2\pi \cdot u_m \left[e^{-\left(\frac{r}{r_u}\right)^2} dr \right]_0^\infty = \pi \cdot u_m \cdot r_u^2 \end{aligned}$$

Thus, this integration over the jet cross section to obtain the flow results in:

$$\frac{d}{ds}(u_m \cdot r_u^2) = 2\alpha \cdot u_m \cdot r_u \quad (8)$$

The continuity equation for the tracer (salt) is:

$$\frac{d}{ds} \left\{ \int_0^\infty c \cdot u \cdot 2\pi \cdot r \cdot dr \right\} = 0 \quad (9)$$

The development of equation (9) yields:

$$\begin{aligned} \int_0^\infty c \cdot u \cdot 2\pi \cdot dr &= \int_0^\infty c_m \cdot e^{-\left(\frac{r}{r_c}\right)^2} \cdot u_m \cdot e^{-\left(\frac{r}{r_u}\right)^2} \cdot 2\pi \cdot r \cdot dr = \\ &= 2\pi \cdot c_m \cdot u_m \int_0^\infty r \cdot e^{-\left(\frac{1}{r_c^2} + \frac{1}{r_u^2}\right) \cdot r^2} dr = \\ &= 2\pi \cdot c_m \cdot u_m \left[e^{-\left(\frac{1}{r_c^2} + \frac{1}{r_u^2}\right) \cdot r^2} \cdot \left(-\frac{1}{2}\right) \cdot \left(\frac{1}{r_c^2} + \frac{1}{r_u^2}\right) \right] = \\ &= \pi \cdot c_m \cdot u_m \cdot \frac{r_u^2}{1 + \left(\frac{r_u}{r_c}\right)^2} = \pi \cdot c_m \cdot u_m \cdot \frac{r_u^2}{1 + \frac{1}{\lambda^2}} = \\ &= \pi \cdot c_m \cdot r_m^2 \cdot \frac{\lambda^2}{1 + \lambda^2} \cdot u_m \end{aligned}$$

Ultimately, the quantity of tracer is constant in the jet, if the ambient contains no tracer, implying that this quantity is equal to what is entering at the jet exit into the ambient:

$$\pi \cdot c_m \cdot r_u^2 \cdot u_m \cdot \frac{\lambda^2}{1 + \lambda^2} = m_0 \quad (10)$$

The initial transport of tracer into the ambient (m_0) is:

$$m_0 = Q_0 \cdot C_0 \quad (11)$$

4.2.2 Momentum conservation

The momentum equation in x -direction is:

$$\frac{d}{ds} \left\{ \int_0^\infty \rho \cdot u^2 \cdot \cos\theta \cdot 2\pi \cdot r \cdot dr \right\} = 0 \quad (12)$$

The development of equation (12) yields:

$$\begin{aligned}
 \frac{d}{ds} \int_0^\infty u^2 \cdot 2\pi \cdot \rho \cdot r \cdot \cos \theta \cdot dr &= \frac{d}{ds} \left\{ 2\pi \cdot \rho \int_0^\infty u_m^2 \cdot e^{-2\left(\frac{r}{r_u}\right)^2} r \cdot \cos \theta \cdot dr \right\} = \\
 &= \frac{d}{ds} \left\{ 2\pi \cdot \rho \cdot u_m^2 \cdot \cos \theta \int_0^\infty r \cdot e^{-2\left(\frac{r}{r_u}\right)^2} dr \right\} = \\
 &= \frac{d}{ds} \left\{ 2\pi \cdot \rho \cdot u_m^2 \cdot \cos \theta \left[e^{-2\left(\frac{r}{r_u}\right)^2} \cdot \left(-\frac{1}{4}\right) \cdot r_u^2 \right]_0^\infty \right\} = \\
 &= \frac{d}{ds} \left\{ \frac{1}{2} \pi \cdot \rho \cdot u_m^2 \cdot r_u^2 \cdot \cos \theta \right\}
 \end{aligned}$$

The horizontal momentum is constant because there is no net force which affects it. Consequently the x -direction momentum is equal to the initial momentum (M_{0x}):

$$\frac{1}{2} \pi \cdot \rho \cdot u_m^2 \cdot r_u^2 \cdot \cos \theta = M_{0x} \quad (13)$$

The initial momentum in the x -direction is determined from:

$$M_{0x} = \rho_0 \cdot \frac{Q_0^2}{A_0} \cdot \cos \theta_0 \quad (14)$$

The vertical momentum equation is expressed as:

$$\frac{d}{ds} \left\{ \int_0^\infty \rho \cdot u^2 \cdot \sin \theta \cdot 2\pi \cdot r \cdot dr \right\} = F'_B \quad (15)$$

The development of left part of equation (15) gives:

$$\begin{aligned}
 \frac{d}{ds} \int_0^\infty u^2 \cdot 2\pi \cdot \rho \cdot r \cdot \sin \theta \cdot dr &= \frac{d}{ds} \left\{ 2\pi \cdot \rho \int_0^\infty u_m^2 \cdot e^{-2\left(\frac{r}{r_u}\right)^2} r \cdot \sin \theta \cdot dr \right\} = \\
 &= \frac{d}{ds} \left\{ 2\pi \cdot \rho \cdot u_m^2 \cdot \sin \theta \int_0^\infty r \cdot e^{-2\left(\frac{r}{r_u}\right)^2} dr \right\} = \\
 &= \frac{d}{ds} \left\{ 2\pi \cdot \rho \cdot u_m^2 \cdot \sin \theta \left[e^{-2\left(\frac{r}{r_u}\right)^2} \cdot \left(-\frac{1}{4}\right) \cdot r_u^2 \right]_0^\infty \right\} = \\
 &= \frac{d}{ds} \left\{ \frac{1}{2} \pi \cdot \rho \cdot u_m^2 \cdot r_u^2 \cdot \sin \theta \right\}
 \end{aligned} \quad (16)$$

F'_B is the vertical buoyancy force acting on the jet. It depends on ambient water density, jet density, and gravity. Figure 13 illustrates a small section of the jet as a definition sketch to how F'_B is calculated.

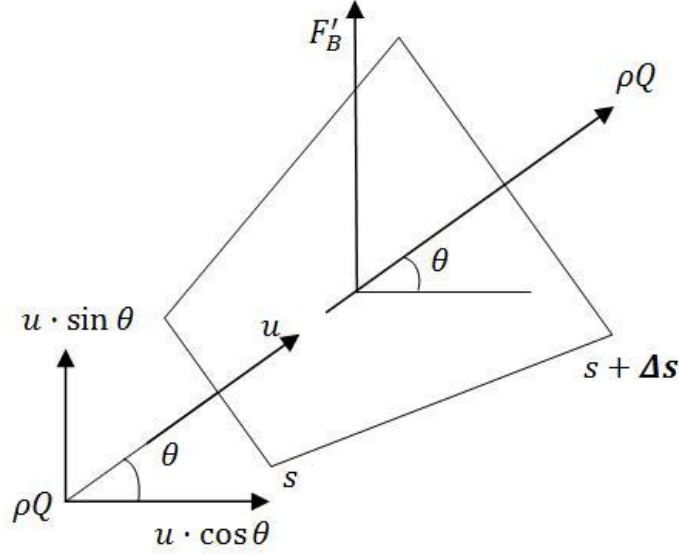


Figure 13 Definition sketch for determining the buoyancy force on a circular jet

The buoyancy force (F'_B) is determined from:

$$F'_B = - \int_0^{\infty} g \cdot (\rho_a - \rho) \cdot 2\pi \cdot r \cdot dr \quad (17)$$

Inserting equation (6) into equation (17), the equation for F'_B becomes:

$$\begin{aligned} F'_B &= - \int_0^{\infty} g \cdot k \cdot c \cdot 2\pi \cdot r \cdot dr = -2\pi \cdot g \cdot k \int_0^{\infty} r \cdot c_m \cdot e^{-\left(\frac{r}{r_c}\right)^2} dr = \\ &= -2\pi \cdot g \cdot k \cdot c_m \cdot \left[e^{-\left(\frac{r}{r_u}\right)^2} \cdot \left(-\frac{1}{2}\right) \cdot r_c^2 \right]_0^{\infty} = \\ &= -\pi \cdot g \cdot k \cdot c_m \cdot r_c^2 \end{aligned} \quad (18)$$

Finally, combining equations (16) and (18), the following equation is obtained:

$$\begin{aligned} \frac{d}{ds} \left(\frac{1}{2} \pi \cdot \rho \cdot u_m^2 \cdot r_u^2 \cdot \sin\theta \right) &= -\pi \cdot g \cdot k \cdot c_m \cdot r_c^2 \\ \frac{d}{ds} (u_m^2 \cdot r_u^2 \cdot \sin\theta) &= -2 \cdot g \cdot \frac{k}{\rho_a} \cdot c_m \cdot r_c^2 \\ \frac{d}{ds} (u_m^2 \cdot r_u^2 \cdot \sin\theta) &= -2 \cdot g \cdot \frac{k}{\rho_a} \cdot c_m \cdot r_u^2 \cdot \lambda^2 \end{aligned} \quad (19)$$

4.2.3 Solution of governing equations

In summary, the governing equations for the model are:

$$\frac{d}{ds}(u_m \cdot r_u^2) = 2\alpha \cdot u_m \cdot r_u \quad (8)$$

$$\pi \cdot c_m \cdot r_m^2 \cdot u_m \cdot \frac{\lambda^2}{1+\lambda^2} = m_0 \quad (10)$$

$$m_0 = Q_0 \cdot C_0 \quad (11)$$

$$\frac{1}{2} \pi \cdot \rho \cdot u_m^2 \cdot r_u^2 \cdot \cos\theta = M_{0x} \quad (13)$$

$$M_{0x} = \rho_0 \cdot \frac{Q_0^2}{A_0} \cdot \cos\theta_0 \quad (14)$$

$$\frac{d}{ds}(u_m^2 \cdot r_u^2 \cdot \sin\theta) = -2 \cdot g \cdot \frac{k}{\rho_a} \cdot c_m \cdot r_u^2 \cdot \lambda^2 \quad (19)$$

Finally, there are two equations defining the geometry of the jet:

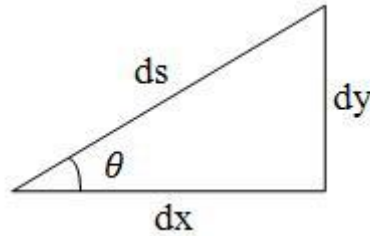


Figure 14 Definition sketch of geometric quantities for the jet

$$\frac{dx}{ds} = \cos\theta \quad (22)$$

$$\frac{dy}{ds} = \sin\theta \quad (23)$$

4.2.4 Solving the governing equation

The system of equations to be solved consists of a set of ordinary differential equations. These equations were solved numerically using finite differences (equation 24), to approximate equations (8), (10), (13), (19), (22) and (23) by small differentials. Therefore, the main idea is to discretize the equations using small steps according to:

$$f'(x) = \frac{f(x+s) - f(x)}{\Delta s} \quad (24)$$

Combining equations (8), (10), (13), (19), (22), (23), and (25) it is possible to obtain the following system of difference equations:

$$\theta_{i+1} = \arctan\left(\tan(\theta_i) - \frac{g \cdot k \cdot \lambda^2 \cdot \pi \cdot \rho}{\rho_a \cdot M_{0x}} \cdot \Delta s \cdot c_{m_i} \cdot r_{u_i}^2\right) \quad (25)$$

$$c_{m_{i+1}} = \frac{1}{\frac{1}{c_{m_i}} + \frac{2 \cdot \alpha \cdot \pi \cdot \lambda^2}{m_0 \cdot (1 + \lambda^2)} \cdot \Delta s \cdot u_{m_i} \cdot r_{u_i}} \quad (26)$$

$$u_{m_i} = \frac{2 \cdot M_{0x} \cdot \lambda^2 \cdot c_{m_i}}{\rho \cdot m_0 \cdot (1 + \lambda^2) \cos \theta} \quad (27)$$

$$r_{u_i} = \frac{m_0 \cdot (1 + \lambda^2)}{\lambda^2 \cdot c_{m_i}} \cdot \sqrt{\frac{\rho \cdot \cos \theta}{2\pi \cdot M_{0x}}} \quad (28)$$

$$x_{i+1} = x_i + \Delta s \cdot \cos \theta_{i+1} \quad (29)$$

$$y_{i+1} = y_i + \Delta s \cdot \sin \theta_{i+1} \quad (30)$$

Where:

i is the number of a specific iteration. Thus, from the jet exit, where all the parameter values are known, the solution proceeds stepwise along the jet, where values at $i+1$ is obtained from the known values at i .

4.3 Sensitivity analysis

The main parameters were changed to analyze the trajectory behavior predicted by the model. These parameters were: iteration step size, entrainment coefficient, initial velocity of the jet, initial concentration of the jet, and nozzle angle. In the following graphs, x and y are the horizontal and the vertical coordinate of the jet trajectory.

First, it is essential to determine the appropriate step size in the numerical solution and how it affects the result. This analysis is important, because if there are no large differences between solutions with different step size, the larger steps should be used. Large steps mean much less calculation time in the computer.

It is possible to observe in Figure 15 the influence of the step size on the shape of the jet trajectory (centerline).

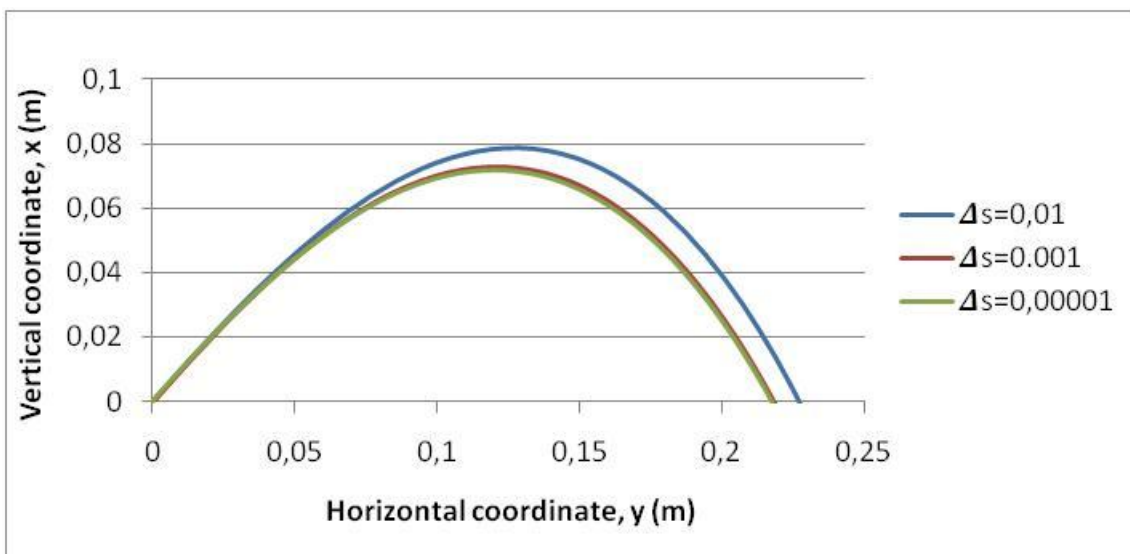


Figure 15 The effect of calculation step size Δs on the jet trajectory

The centerlines are stable and they do not exhibit any irregularities. The use of a too large step implies some errors; however, when small enough steps are utilized, the centerlines are very similar. One possibility to check if the selected step size is correct is by calculating for two different step sizes and check how similar the final results are.

Also, it is important to check how sensitive the model is towards different values on the entrainment coefficient. This parameter quantifies at what rate water from the ambient enters into the jet. The standard value is around 0.0585 for jets (Fischer, 1979). Figure 16 shows the results for the standard value, two limit values (0.0485 and 0.0585), and two extreme limit values (0.0435 and 0.0635) on the entrainment coefficient. These last two values are larger than normal, but they are shown to give an idea of how more extreme differences in the entrainment coefficient influence the result. In conclusion, the entrainment coefficient does not affect the results a lot in the model.

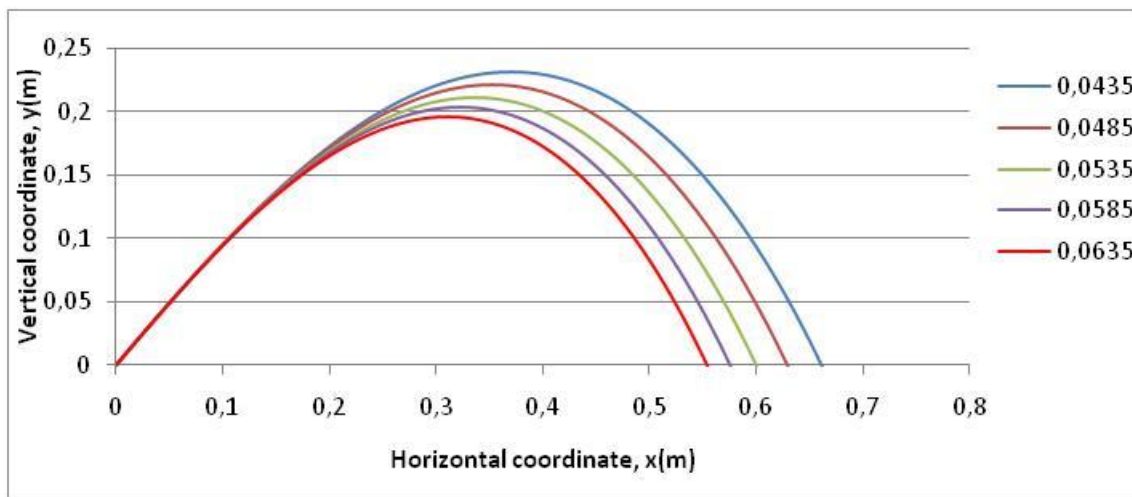


Figure 16 The effect of entrainment coefficient on the jet trajectory

Figure 17 shows how the jet trajectory changes depending on different initial velocities. Larger velocities produce trajectories that are longer compared to smaller velocities; therefore, using larger velocities the dilution rates will be larger. On the other hand, the energy necessary to create the jet will be larger as well. A large difference may be observed between small and large velocities.

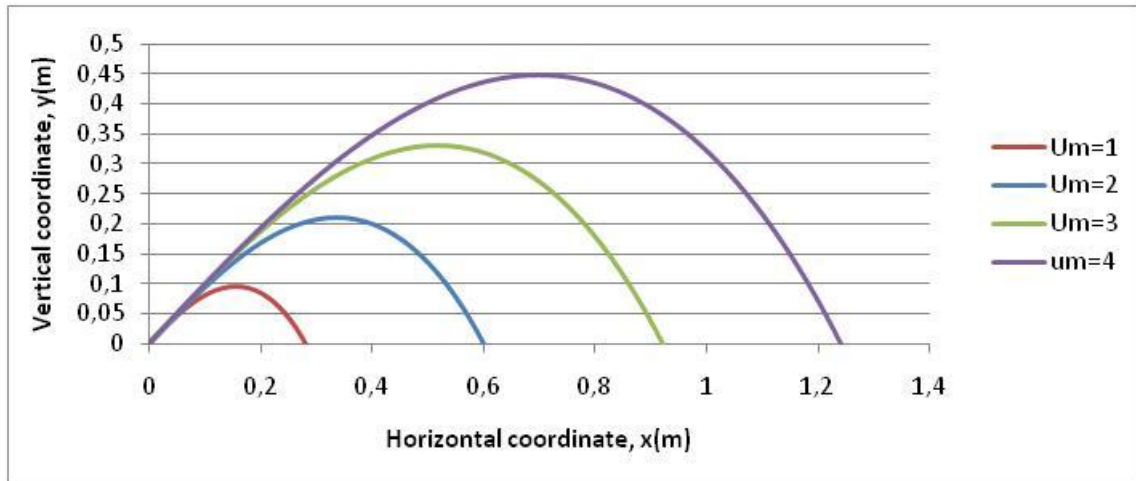


Figure 17 The effect of initial velocity on the jet trajectory

Using different initial concentrations imply having different initial densities in the jet. Larger salinities involve shorter trajectories due to the negative buoyancy effect, because heavier water reaches the sea bed faster than lighter water.

In Figure 18 trajectories with different initial concentration are displayed and there are significant differences in the trajectory length between the different salinities. The corresponding dilution rates in this case are 29.4 for 2% salinity, 20.5 for 4%, and 16.6% for 6%. It is easy to conclude the opposite behavior, because when there are large differences between the ambient water concentration and jet water concentration, the dilution rate should be larger due to the fact that the density difference are larger; however, it is necessary to take into account that the trajectory with low salinity is longer than the one for high salinity yielding a larger mixing.

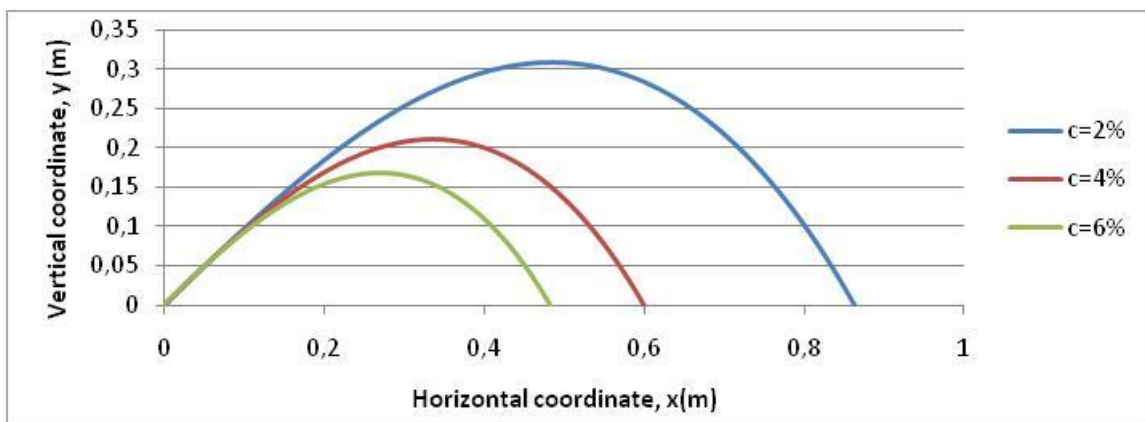


Figure 18 The effect of initial concentration on the jet trajectory

Figure 19 shows the variation in trajectory shape depending on the angle of the nozzle (defines the initial direction of discharge). The longer the jet trajectory is, the better the dilution rate will be. Thus, in the case where the slope of the sea bottom is zero, the optimum case is when the initial angle of the nozzle is 60° . If there is a slope in the sea bottom, the angle should be decreased to obtain the longest trajectory possible.

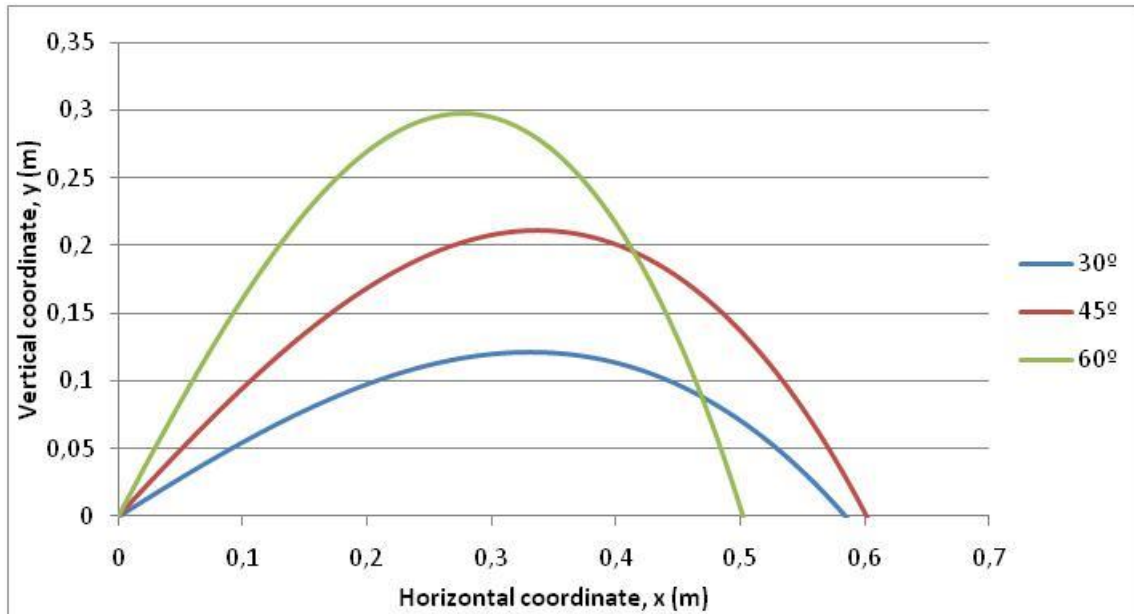


Figure 19 The effect of nozzle angle (initial direction of discharge) on the jet trajectory

5. Non-dimensional analysis

It is highly useful to have an easy method to calculate the maximum height of the jet (y_m), where this height occurs along the horizontal axis (x_m), and the dilution rate (S_m) in the point where the jet impinges on the sea bottom (jet quantities at the centerline are studied). One way to achieve this is by solving the equations expressed in non-dimensional form and generating figures from which the quantities of interest can be easily obtained.

First, it is necessary to decide which variables should be fixed at the start of the calculation and from which the remaining variables will be determined. For example, it is possible to fix the dilution rate and look for the optimum solution for a certain water depth and initial nozzle angle.

In order to develop general results, it is efficient to put the equations in non-dimensional form and to select quantities for the normalization of the equations. Candidate quantities for his normalization would involve the initial volume, momentum, and buoyancy flux, as well as certain geometric properties of the jet such as nozzle diameter.

5.1 Governing equations

The governing equations are first expressed in terms of volume flux, momentum flux, and tracer flux. The definition of the variables used in this section is the same as in section 4.

The flow is given by:

$$Q = \pi \cdot u_m \cdot r_u^2 \quad (31)$$

The momentum flux is expressed as:

$$M = \frac{1}{2} \cdot \pi \cdot \rho \cdot u_m^2 \cdot r_u^2 \quad (32)$$

Combining equations (8) and (31) yields:

$$\frac{dQ}{ds} = 2\sqrt{2\pi} \cdot \alpha \cdot \sqrt{\frac{M}{\rho}} \quad (33)$$

Then, combining equations (10) and (31) gives:

$$c_m = \frac{1+\lambda^2}{\lambda^2} \cdot \frac{m_0}{Q} \quad (34)$$

From equations (13) and (32) the following relationship is obtained:

$$M \cdot \cos \theta = M_{0x} \quad (35)$$

Combining equations (21) and (32) yields:

$$\frac{d}{ds}(M \cdot \sin \theta) = -\frac{1}{2} \cdot \rho_a \cdot K \cdot \lambda^2 \cdot c_m \cdot \frac{Q^2}{M} \quad (36)$$

To normalize equations (33), (34), (35), and (36), the following definitions are introduced:

$$S' = \frac{S}{Q_0} \sqrt{\frac{M_0}{\rho}} \quad (37)$$

$$M' = \frac{M}{M_0} \quad (38)$$

$$Q' = \frac{Q}{Q_0} \quad (39)$$

$$c'_m = \frac{c_m}{c_{m0}} \quad (40)$$

Combining equations (33), (34), (35), and (36) and normalizing using equations (37), (38), (39), and (40), the following equations are obtained:

$$\frac{dQ'}{ds'} = 2\sqrt{2\pi} \cdot \alpha \cdot \sqrt{M'} \quad (41)$$

$$c'_m = \frac{1}{Q'} \quad (42)$$

$$M' \cdot \cos \theta = \cos \theta_0 \quad (43)$$

$$\frac{d}{ds'}(M' \cdot \sin \theta) = -2\sqrt{2\pi} \cdot \lambda^2 \cdot \frac{1}{F_0^2} \cdot c'_m \cdot \frac{Q'^2}{M'} \quad (44)$$

Where F_0 is the densimetric Froude number.

Also, it is necessary to express the geometric relationships from equations (22) and (23) in non-dimensional form:

$$\frac{dx'}{ds'} = \cos \theta \quad (45)$$

$$\frac{dy'}{ds'} = \sin \theta \quad (46)$$

The horizontal and vertical coordinates, respectively, are expressed in non-dimensional form as follows:

$$x' = \frac{x}{Q_0} \sqrt{\frac{M_0}{\rho}} \quad (47)$$

$$y' = \frac{y}{Q_0} \sqrt{\frac{M_0}{\rho}} \quad (48)$$

Using the same solution scheme as when solving the dimensional system of equations, it is possible to apply equation (24) to calculate the results using small steps in the difference equations. The final result is:

$$\theta_{i+1} = \arctan \left(\tan \theta_i - 2\sqrt{2\pi} \cdot \lambda^2 \cdot \frac{2}{\cos \theta_0 \cdot F_0^2} \cdot c_{m_i} \cdot \frac{Q_i^2}{M_i} \cdot \Delta s' \right) \quad (49)$$

$$c_{m_{i+1}} = \frac{1}{2\sqrt{2\pi} \cdot \alpha \cdot \sqrt{M_i' + \frac{1}{c_{m_i}}}} \quad (50)$$

$$M_{i+1} = \frac{\cos \theta_0}{\cos \theta_{i+1}} \quad (51)$$

$$Q'_{i+1} = \frac{1}{c_{m_{i+1}}} \quad (52)$$

$$x'_{i+1} = x'_i + \Delta s' \cdot \cos \theta_{i+1} \quad (53)$$

$$y'_{i+1} = y'_i + \Delta s' \cdot \sin \theta_{i+1} \quad (54)$$

5.2 Non-dimensional engineering properties

Figure 20, Figure 21, and Figure 22 show how the non-dimensional variables x_m' , y_m' , and S_m vary depending on the densimetric Froude number and initial nozzle angle (subscript m refers to maximum).

Based on the results in Figure 20, it is possible to presume that there is a linear relationship between the densimetric Froude number and x_m' for each initial nozzle angle. It is observed that the longest x_m' for a fixed Froude number occurs when the initial nozzle angle is 30° or 45°. The result is the same for 30° and 45°. It is also possible to observe that x_m' is longer for a fixed initial nozzle angle when the Froude number is larger due to larger initial velocity or smaller density differences between the ambient and jet water.

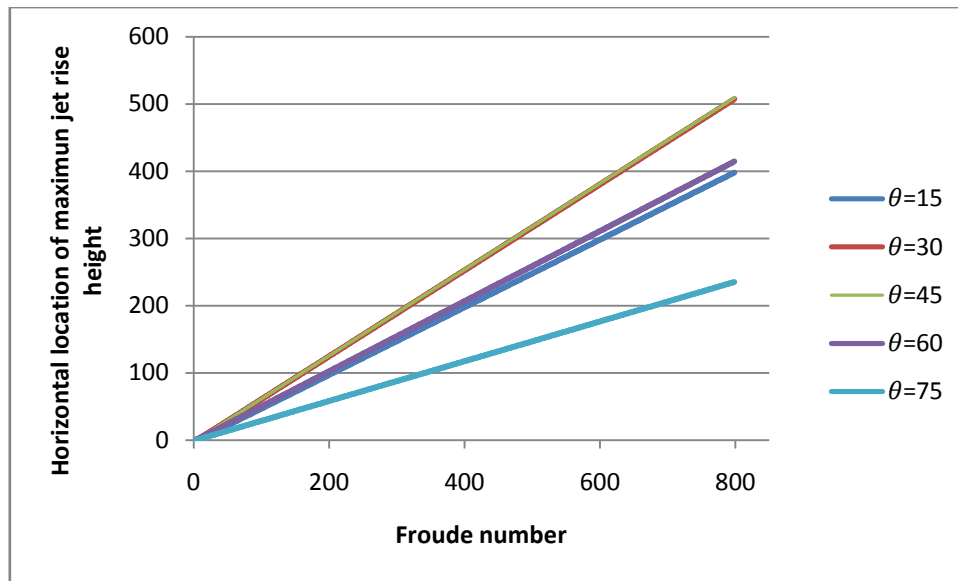


Figure 20 Horizontal location of maximum jet rise height as a function of densimetric Froude number for different initial nozzle angles

In Figure 21 it can be observed how y_m' varies with the initial nozzle angle and the densimetric Froude number. As expected, a larger Froude number or a larger initial nozzle angle produces a larger y_m' due to the larger initial vertical momentum flux that is obtained under these conditions.

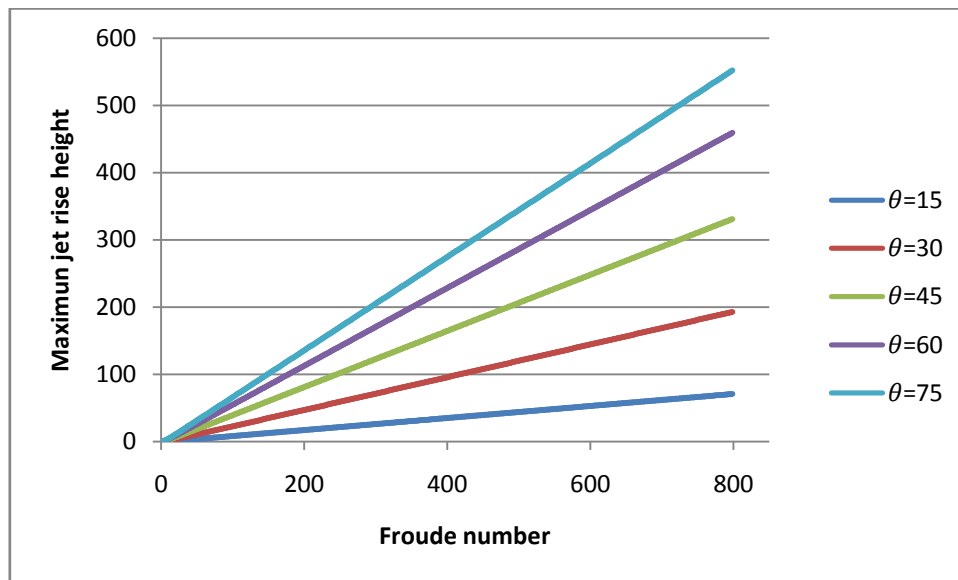


Figure 21 Maximum jet rise height as a function of densimetric Froude number for different initial nozzle angles

Finally, Figure 22 shows how the dilution rate changes when initial nozzle angle and Froude number change. When the Froude number is large, which implies that the velocity is large or the density difference is small, the dilution rate is larger due to the larger trajectory which the jet follows. It can also be seen that the maximum dilution rate occurs when initial nozzle angle

is 45°, 60° and 75° when the Froude number is less than 350. However, when the Froude number is larger than 350, an initial nozzle angle 60° is the best option. Overall, the difference between 60 degrees and the other two nozzle angles (45° and 75°) is small. In the practical case, the 75-degrees case will normally not be used in order to avoid a large jet height.

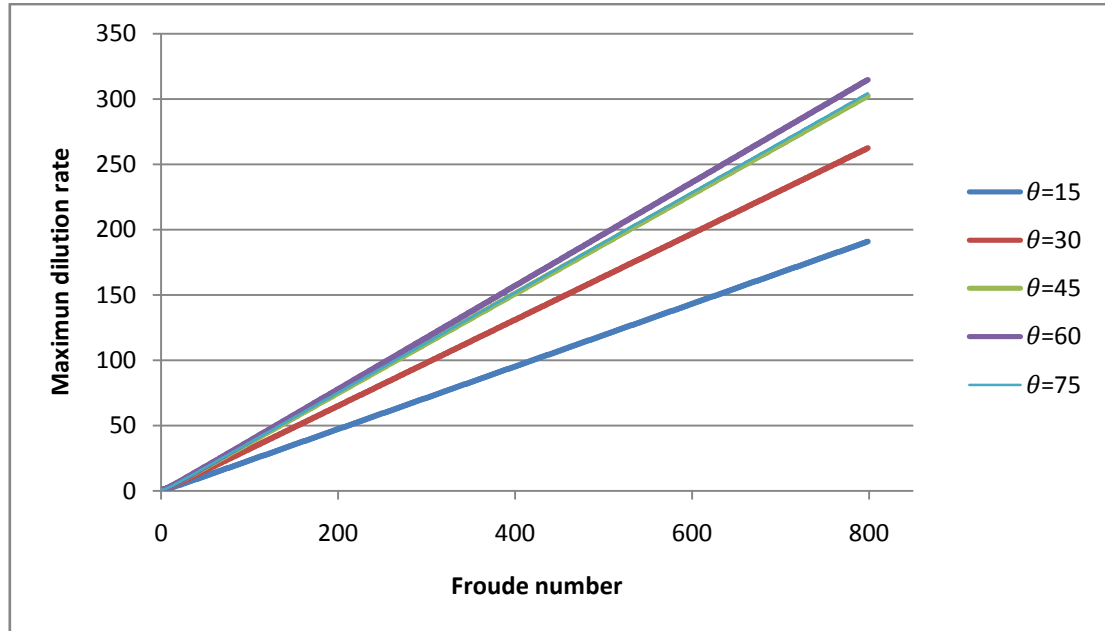


Figure 22 Maximum dilution rate as a function of densimetric Froude number for different initial nozzle angles

5.3 Non-dimensional engineering properties using realistic Froude numbers

Froude number was calculated for realistic flow situations to check whether the results presented in Figure 20, Figure 21, and Figure 22 can be delimited. The densimetric Froude number is defined as:

$$Fr = \frac{u_0}{\sqrt{g \frac{\rho_a - \rho_0}{\rho_0} \cdot D}} \quad (55)$$

The velocity is typically between 1 m/s and 4 m/s, the diameter between 10 cm and 50 cm, and the density of the ambient and the jet 1040 kg/m³ and 1080 kg/m³, respectively. These values are common in design and analysis situations for field conditions. It can be observed in Table 1 that the maximum Froude number is 21 for these input values.

Table 1 Froude number for real situations

Velocity (m/s)	Diameter (m)	Fr
1	0,1	5,2
1	0,2	3,6

1	0,3	3,0
1	0,4	2,6
1	0,5	2,3
2	0,1	10,3
2	0,2	7,3
2	0,3	5,9
2	0,4	5,2
2	0,5	4,6
3	0,1	15,5
3	0,2	10,9
3	0,3	8,9
3	0,4	7,7
3	0,5	6,9
4	0,1	20,6
4	0,2	14,6
4	0,3	11,9
4	0,4	10,3
4	0,5	9,2

Based on this assessment of the Froude number during field conditions, it is possible to estimate the maximum Froude number to be about 30, and a more detailed description of the parameter behavior may be derived. It is seen that for small Froude numbers the relationships are not close to linear, as was the case for the range of larger Froude numbers.

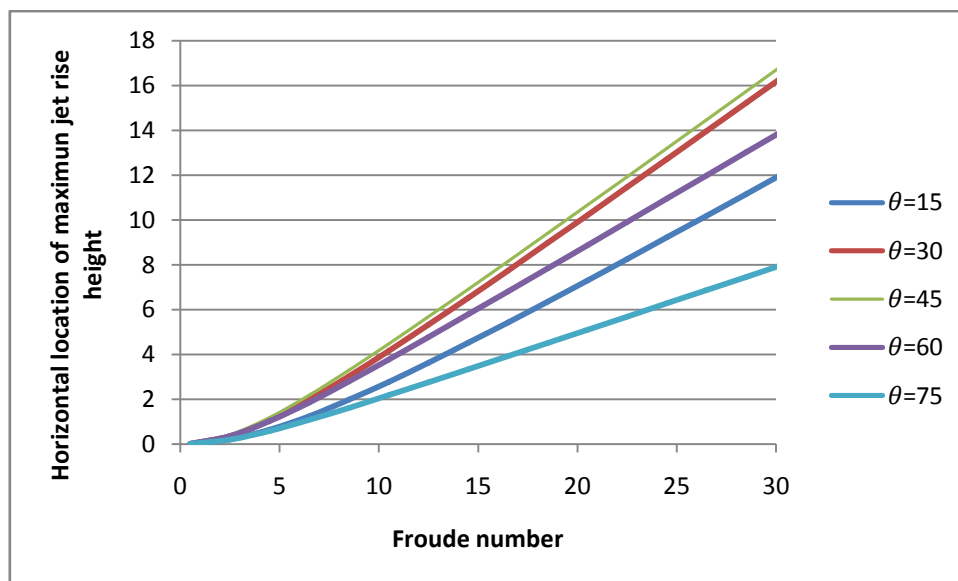


Figure 23 Horizontal location of maximum jet rise height as a function of densimetric Froude number for different initial nozzle angles for a lower Froude number range

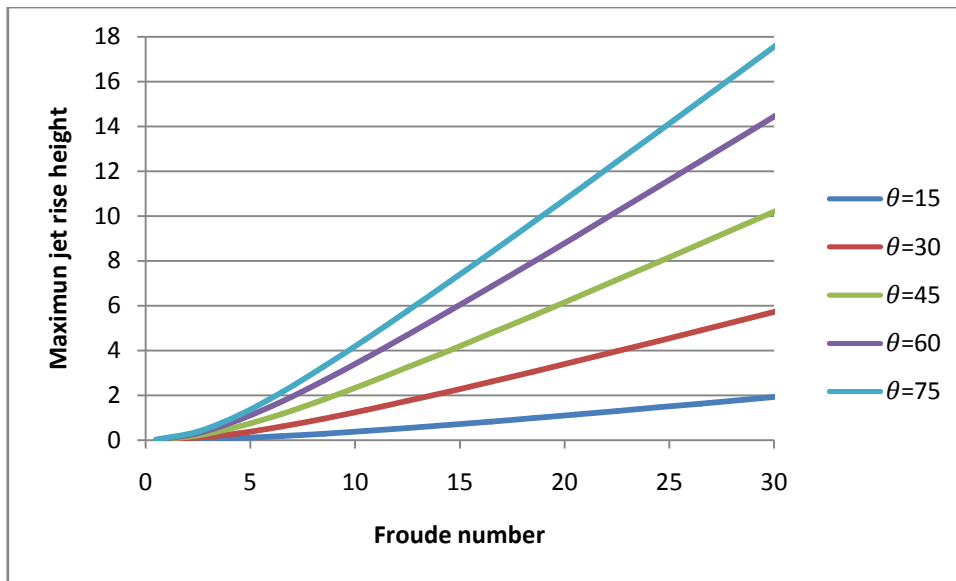


Figure 24 Maximum jet rise height as a function of densimetric Froude number for different initial nozzle angles for a lower Froude number range

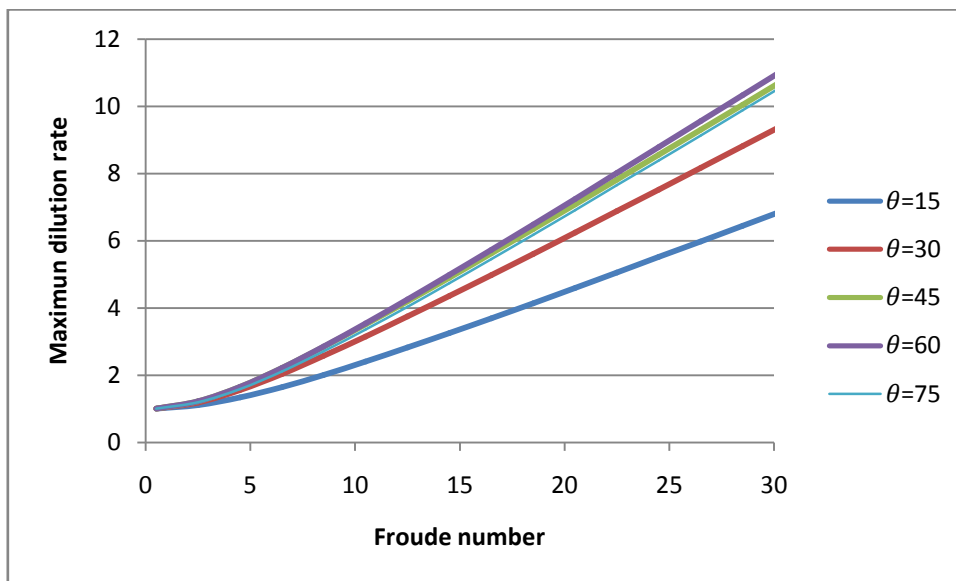


Figure 25 Maximum dilution rate as a function of densimetric Froude number for different initial nozzle angles for a lower Froude number range

6. Laboratory experiments

An experiment was performed in the Water Resources Engineering (TVRL) laboratory on the behavior of a negatively buoyant jet. The main purpose of this experiment was to investigate if the model could accurately represent the evolution of a negatively buoyant jet. In the following, the experimental setup and procedure will be described and the results of the experiment will be compared with model calculations.

6.1 Setup

It was necessary to develop an experimental setup and a measurement system to execute the experiment. A high elevation tank was connected using a plastic hose to a nozzle which was located inside a larger water tank. Between the elevated tank and the nozzle a valve was installed to regulate the flow together with a flow meter to record the flow. Downstream the flow meter, another hose was connected to the principal hose in order to empty all the air from the system before each experimental run.

The main components of the experimental system were:

- Water tanks
- Flow meter and frequency meter
- Pump
- Hoses
- Valves
- Nozzles and nozzle support
- Salt
- Dye

6.1.1 Water tanks

Different material and size tanks were used in the experiment. Some tanks were utilized to mix fresh water (from the tap) and salt to obtain the saline water necessary to create the negatively buoyant jet. Two tanks made of plastic were used and their capacities were 45 liters and 90 liters.

Two other tanks, also made of plastic, each with a volume of about 50 liters, were filled up with the saline water that was dyed and placed at a higher elevation compared to the main experimental tank. This elevation difference was used to create the hydraulic head needed to generate the jet in the main tank. These two tanks were connected by a hose to obtain a larger capacity and therefore a smaller water level variation when water was discharged during an

experimental run. The two tanks with the saline water had a connection between them consisting of a plastic tube. The tanks can be seen at the top on the right side in Figure 26 or on the top in Figure 27.

The main experimental tank was made of glass and was filled with fresh water from the tap prior to an experimental run. The saline water was introduced through a nozzle at the bottom of the tank and it was dyed to allow for easy observation of the jet evolution inside the tank. The main tank had a capacity of about 500 liters. First, a longer tank was employed in the experiment that had a smaller depth, but in some of the experimental runs the jet hit the water surface. In order to avoid this jet impact, another deeper tank was acquired. This tank is shown in the center of Figure 26.



Figure 26 Water tanks used in the experiment on negatively buoyant jets

6.1.2 Flow meter and frequency meter

A flow meter was used to measure the quantity of flow in the hose between the high-position tanks and the nozzle. The flow meter needed a frequency meter which was connected using an electronic circuit, which was specifically developed for that purpose. The frequency recorded is proportional to the flow. The measurement system was calibrated before being used in the experiment. The flow meter may be seen on the left in Figure 27 and the frequency meter on the right.



Figure 27 Flow meter and tanks for saline water used in the experiment

6.1.3 Pump

A submersible pump was used to empty the water in the main tank after an experimental run, since there was no outlet from the tank. The maximum pump flow was 3600 liters per hour; therefore around 12 minutes was needed to empty all the water in the main tank.

The pump was also used to lift the saline water to the high-elevation tanks, because the saline water was prepared at a lower level that was comfortable to work at.

6.1.4 Hoses

A 15-mm diameter plastic hose was used to connect the high elevation tank with the nozzle, including the circuit to remove the air from the pipe.

Another hose, which was 25 mm in diameter, was used to connect to the tap, where water was taken to fill the main tank. The same hose was used to subsequently empty the main tank after an experimental run using the pump to discharge to a sink.

6.1.5 Valves

Two valves were used in the experiments. The first one was utilized to regulate the water flow between the high-elevation tanks and the nozzle inside the main tank. The other one was used to open and close the circuit to remove the air. The valves are shown in Figure 28.

Prior to an experimental run, the hose contained significant amounts of air, which was difficult to evacuate, taking a long time. So, a special hose was used to get rid of the air. The nozzle opening was blocked with a finger and the flow control valve was open. After these two actions, the other valve was opened and all the air could leave through the open hose. Some light vibration was applied to the hose system so that the air evacuated faster. Once all the air was removed, the two valves were closed again.

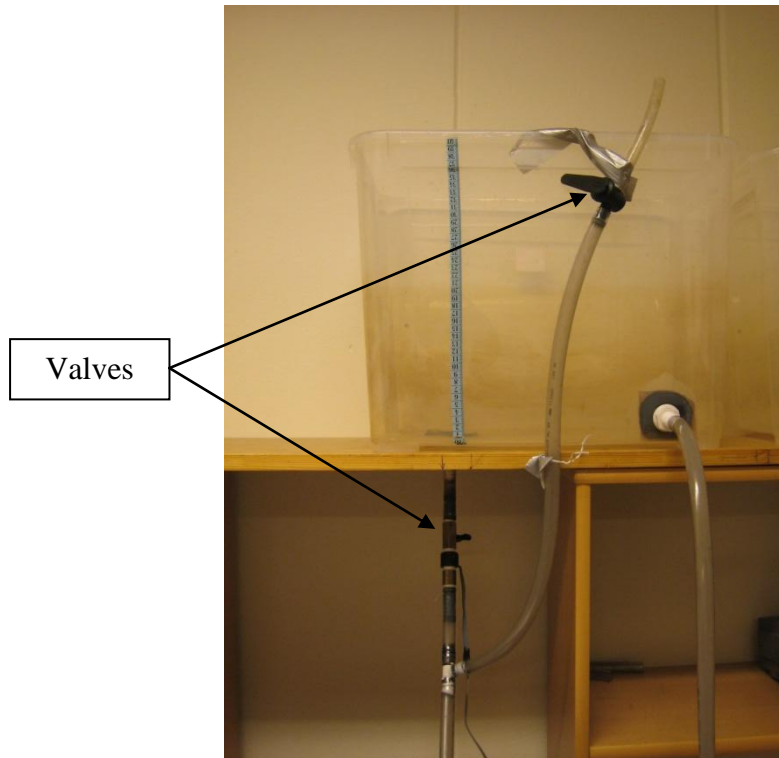


Figure 28 Valves utilized for flow control and air evacuation

6.1.6 Nozzles and nozzle support

A nozzle was used to inject saline water into the fresh water, which was stored in the main tank. Nozzles of different sizes were employed in the experiment in order to investigate the influence of the diameter on the jet evolution. The diameters used were 1.5 mm, 2.3 mm, 3.3 mm, and 4.8 mm. The nozzles were attached to an inclined pipe section to obtain different initial jet angles, as shown in Figure 29.

A support system was created to firmly attach the nozzle and the inclination selector to the bottom of the main tank. Some suction pads were attached to form the support and to yield a stable position. Suction pads were utilized to have a system which allowed for easy removal and placement.



Figure 29 Nozzle support system on which the nozzle was attached

6.1.6 Salt

Salt was used to create the saline water in the jet by mixing it with fresh water (from the tap). The water quantity was measured using a bucket and the salt was measured using a balance to obtain the correct salt concentration. A concentration sample of saline water was taken for each experimental run and compared with the concentration of a sample with known salinity. The water conductivity was measured in the two samples and compared to check that they were equal, implying the same salinity.

6.1.7 Dye

Potassium permanganate was used to change the color of the saline water in the discharged jet. The dye converted the transparent water into a purple color. The use of a purple jet was made to facilitate the observation of the behavior of the jet in the main tank with fresh water. The concentration of the dye was 0.1 g/liter.

6.2 Procedure

After the nozzle inclination and diameter were selected, the main tank was filled with fresh water, the saline water with the dye was prepared, and the air was removed from the hose. After this, everything was set to start an experimental run.

Two experimental runs could be performed using the same volume of fresh water in the main tank; subsequently, the water in the main tank had to be replaced. First, a low velocity was employed to avoid a large quantity of dye in main tank. The results from the low-velocity run were obtained; then the velocity was increased to record data for a jet with higher velocity. This procedure was used to obtain data for two different jets without replacing the water in the main tank, saving both water and time.

The technique employed to collect the data consisted of drawing lines following the borders of the jet on the frontal glass of the tank. The accuracy of this approach was satisfactory, since a sequence based on drawing and checking was utilized until the lines followed the limiting jet trajectories well. After an experimental run, the centerline of the jet was estimated as a line between the two border lines for the jet. The lines were drawn using a non-permanent marker to easily erase the lines after a run.

Finally, some measurements were obtained from the drawn lines on the glass. These measurements included the maximum centerline point coordinates (x_m, y_m), the maximum point coordinates for the upper border line (x_z, y_z), and largest horizontal distance of the jet (x_i) where it impinges on the horizontal plane (Figure 30).

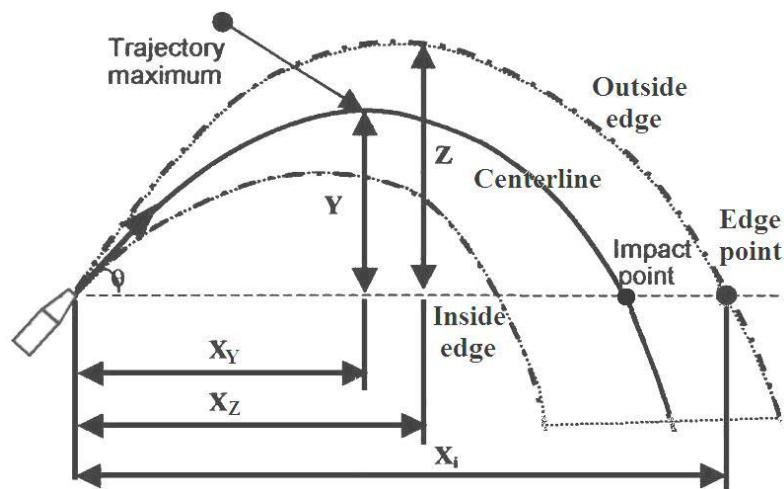


Figure 30 Jet measured parameters

6.3 Observations

The experimental data are summarized in Appendix 1.

6.4 Data analysis

Exploratory analysis was carried out to find some relationships between the different parameters recorded. Initially, the data were analyzed by plotting x_m/D and y_m/D against the Reynolds number to check if the jet was turbulent. Then, x_m/D and y_m/D were plotted against the densimetric Froude number to indicate any possible relationships between these variables.

6.4.1 Reynolds number analysis

Two graphs were developed to investigate whether any relationship existed between x_m/D or y_m/D and the Reynolds number. One of the graph shows results from the experimental runs when Reynolds number were between 2500 and 5000 (in this range the conditions may be

close to laminar or in the transition zone), and the other graph shows results when the Reynolds number were larger than 5000.

Figure 31 shows the relationship between the distance to the location for the maximum height of the jet centerline and the Reynolds number when it is between 2500 and 5000. It may be determined that there is no relationship between the variables, since the correlation coefficient is close to zero. Figure 32 shows the relationship when the Reynolds number is larger than 5000. A weak linear trend may be observed, mainly due to a few outliers, and the correlation coefficient is still quite small (around 0.3), so no firm conclusions about the relationship can be made.

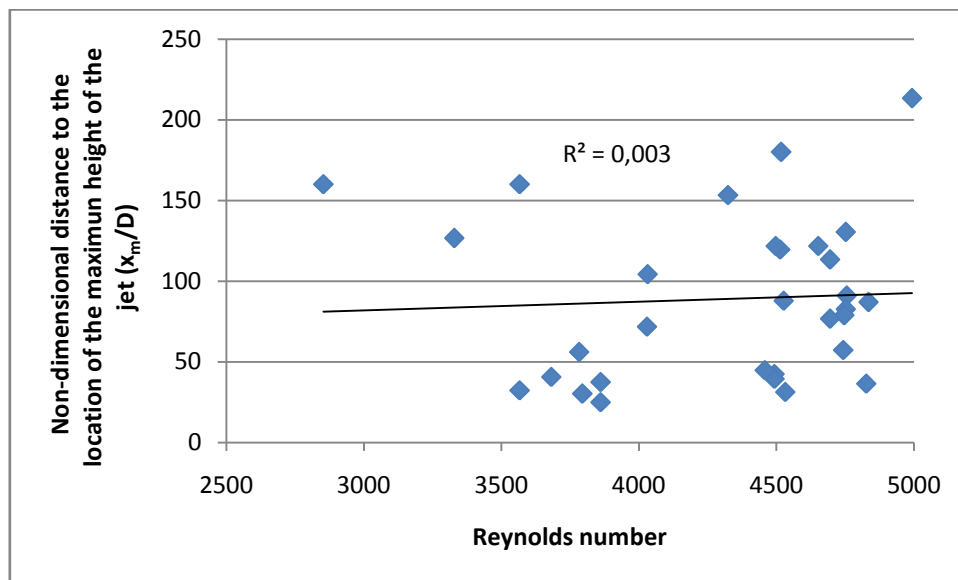


Figure 31 Non-dimensional distance to the location of the maximum height of jet centerline (x_m/D) versus the Reynolds number for the range $2500 < Re_y < 5000$

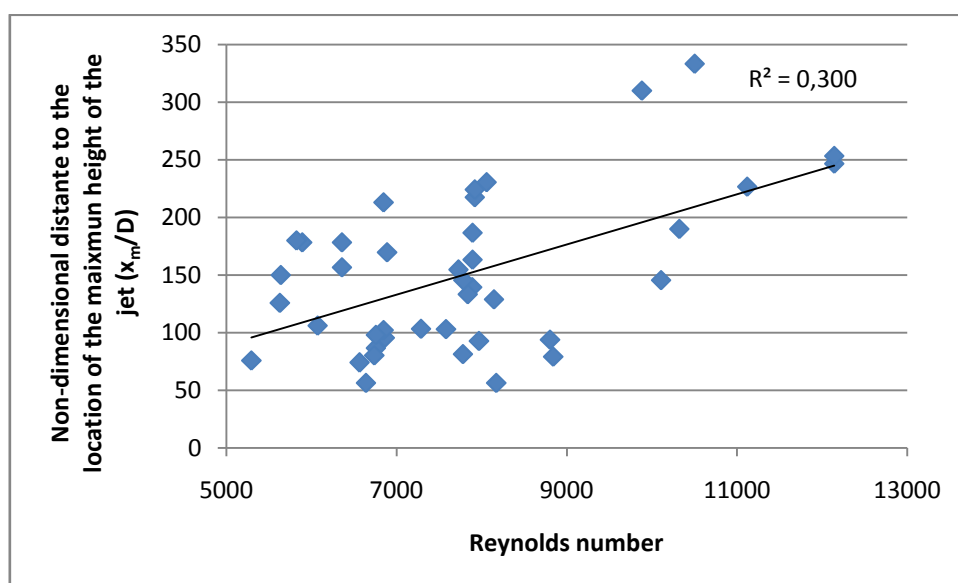


Figure 32 Non-dimensional distance to the location of the maximum height of jet centerline (x_m/D) versus the Reynolds number for the $Re_y > 5000$

Figure 33 shows y_m/D against the Reynolds number with the Reynolds number being between 2500 and 5000, and Figure 34 shows y_m/D against the Reynolds number when it is larger than 5000. It can be assessed that no linear relationship may be found and the correlation coefficient is very small.

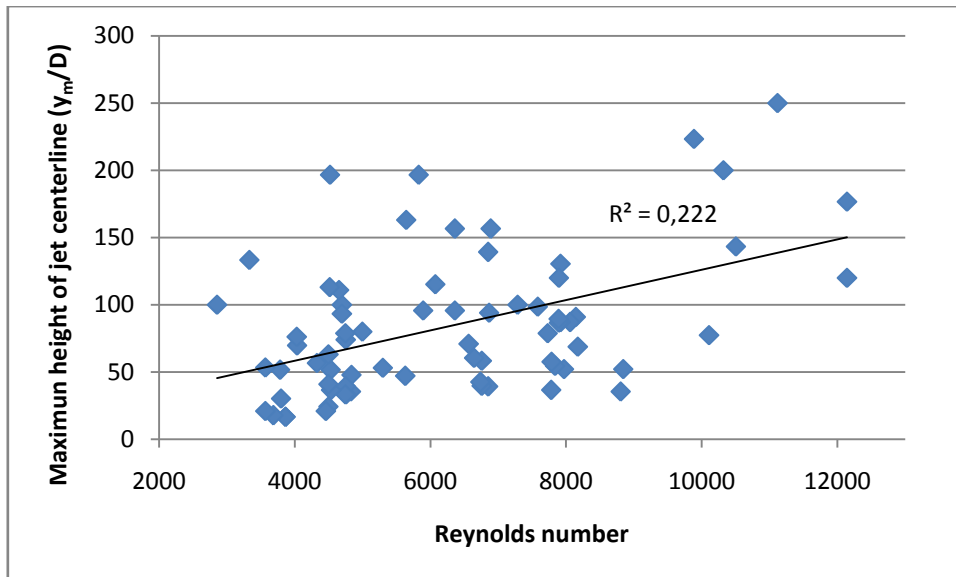


Figure 33 Maximum height of jet centerline (y_m/D) versus Reynolds number ($2500 < \text{Rey} < 5000$)

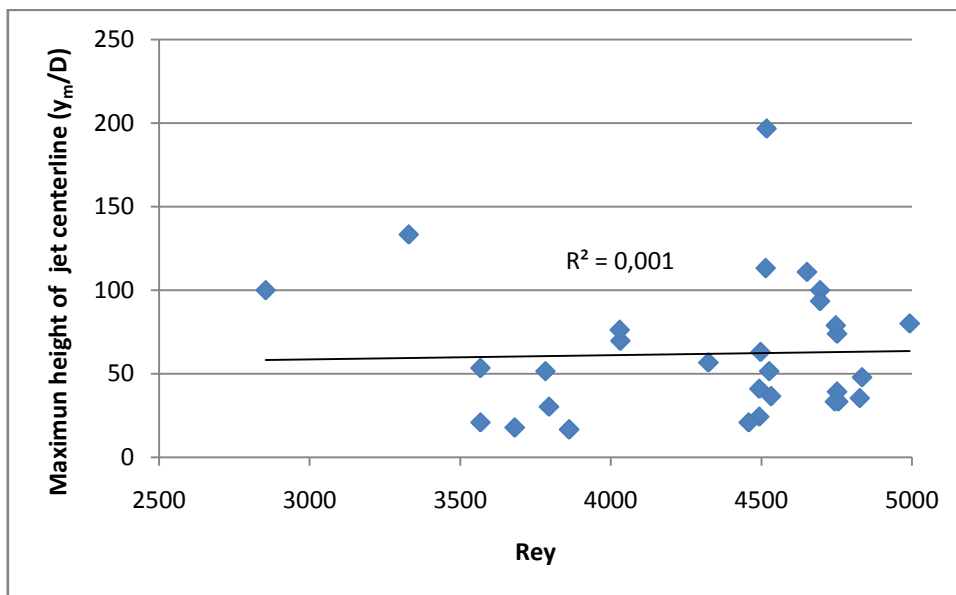


Figure 34 Maximum height of jet centerline (y_m/D) versus Reynolds number ($\text{Rey} > 5000$)

In conclusion, no marked relationship between x_m/D or y_m/D and the Reynolds number was observed in the present experiment.

6.4.2 Densimetric Froude number analysis

Several graphs were made between x_m/D and y_m/D , and the densimetric Froude number to identify possible relationships. The different parameters of interest are the diameter (D), the salinity (S), the and angle of the nozzle (θ). Two of those parameters were fixed in the analysis and the correlation coefficient (R^2) was calculated to check if any linear relationship was present.

Table 2, Table 3, and Table 4 show the correlation coefficients depending on which parameters were fixed for the case when x_m/D versus the Froude number was investigated. The best correlation coefficient was found when the salinity and diameter were fixed. The average correlation coefficient is 0.81. In all the other cases, the correlations are smaller. Figure 35 shows the linear regression when the diameter is 0.0033 m and the salinity takes on three different values (2%, 4%, and 6%). It can also be seen in Table 3 that the correlation coefficient has a tendency to increase with a decrease in diameter.

Table 2 Correlation coefficient for x_m/D versus densimetric Froude number with salinity and initial nozzle angle fixed

S/θ	60	45	30	Average
2	0.7529	0.8079	0.8676	0.8094
4	0.4576	0.6471	0.8156	0.6401
6	0.8761	0.8642	0.9563	0.8989
Average	0.6955	0.7731	0.8798	0.7828

Table 3 Correlation coefficient for x_m/D versus densimetric Froude number with salinity and nozzle diameter fixed

S/D	0.0015	0.0023	0.0033	0.0048	Average
2	0.7525	0.6712	0.9674	0.9079	0.8248
4	0.8146	0.8955	0.8691	0.8571	0.8591
6	0.4704	0.8709	0.8651	0.8135	0.7549
Average	0.6792	0.8125	0.9005	0.8595	0.8129

Table 4 Correlation coefficient for x_m/D versus densimetric Froude number with initial nozzle angle and diameter fixed

θ/D	0.0015	0.0023	0.0033	0.0048	Average
30	0.7464	0.5488	0.16	0.8943	0.5873
45	0.4442	0.4976	0.3508	0.7788	0.51785
60	0.6253	0.2576	0.311	0.8541	0.512
Average	0.6053	0.43467	0.2739	0.8424	0.539

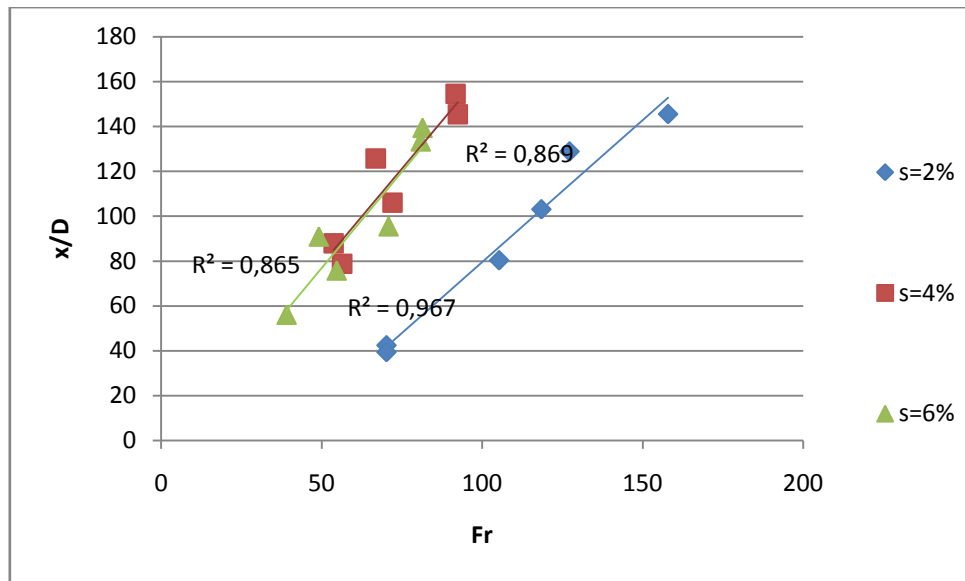


Figure 35 Non-dimensional distance to the location of the maximum height of jet centerline (x_m/D) versus densimetric Froude number ($D = 0.0033$ m).

Table 5, ¡Error! No se encuentra el origen de la referencia., and

Table 7 show the correlation coefficient when y_m/D versus the densimetric Froude are analyzed, keeping two of the three parameters (salinity, initial nozzle angle, and diameter) fixed. In this case the best correlation coefficient is found when the salinity and the initial nozzle angle are fixed, yielding an average value of 0.77. However, relatively poor correlation is observed when the initial nozzle angle is 30°. In ¡Error! No se encuentra el origen de la referencia. and

Table 7 the correlation values are significantly lower.

Table 5 Correlation coefficient y_m/D versus densimetric Froude number fixing salinity and initial nozzle angle

S/θ	60	45	30	Average
2	0,8223	0,8598	0,8519	0,8447
4	0,6804	0,8593	0,2826	0,6074
6	0,944	0,9484	0,6642	0,8522
Average	0,8156	0,8892	0,5996	0,7681

Table 6 Correlation coefficient y_m/D versus densimetric Froude number fixing salinity and nozzle diameter

S/D	0.0015	0.0023	0.0033	0.0048	Average
2	0,7799	0,013	0,5823	0,7507	0,5315
4	0,3762	0,2522	0,0129	0,5533	0,2987
6	0,2682	0,4374	0,4116	0,5362	0,4134
Average	0,4748	0,2342	0,3356	0,6134	0,4145

Table 7 Correlation coefficient y_m/D versus densimetric Froude number fixing initial nozzle angle and diameter

θ/D	0.0015	0.0023	0.0033	0.0048	Average
30	0,8977	0,0344	0,7324	0,9002	0,6412
45	0,3332	0,5435	0,4689	0,842	0,5469
60	0,4641	0,0979	0,2443	0,7383	0,3862
Average	0,565	0,2253	0,4819	0,8268	0,5247

7. Model comparison with data

Predictions by the model developed based on the governing equations for a buoyant jet in an ambient was compared with the data from the present laboratory experiment as well as with data from Cipollina *et al.* (2005).

The comparison was made with regard to the maximum height for the jet centerline and its horizontal position with respect to the nozzle. The overall error between the model and the experimental data was estimated as:

$$\varepsilon = \frac{\left| \frac{x_{model} - x_{experimental}}{x_{experimental}} \right| + \left| \frac{y_{model} - y_{experimental}}{y_{experimental}} \right|}{2} \quad (56)$$

7.1 Comparison between model simulations and experimental data

After completing the laboratory experiment, model simulations were performed in order to compare with the collected data. The result of this comparison is discussed in the following.

7.1.1 Jet trajectory comparison

An entrainment coefficient value of 0.0535 was employed in the model simulations. Appendix 1 summarizes the experimental data (salt concentration, initial nozzle angle, nozzle diameter, flow, horizontal distance to maximum centerline height and maximum centerline height), the result of the model simulation (horizontal distance to maximum centerline height and maximum centerline height), and the calculated error according to equation (56).

The obtained errors are quite large using this value on the entrainment coefficient. The average error for the 72 experiments, when comparing the results from the model simulations with the data, is almost 0.4. Figure 36 shows error distribution.

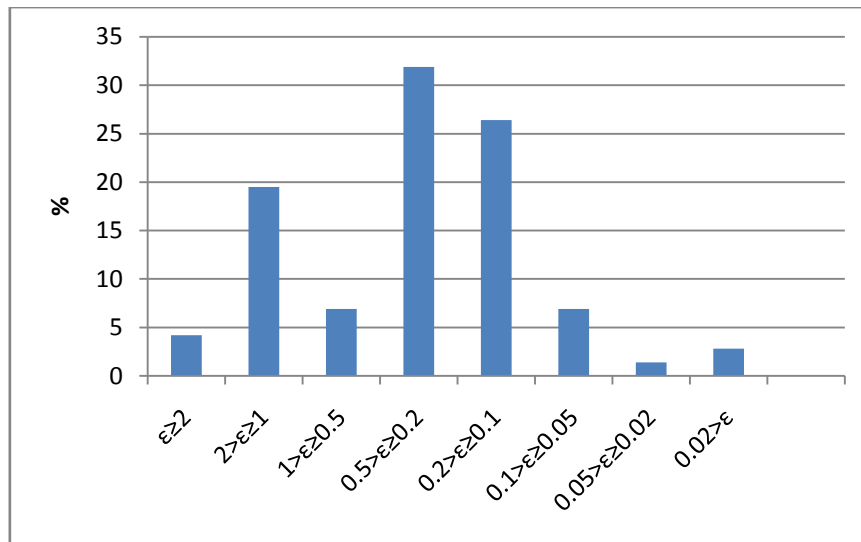


Figure 36 Distribution of simulation errors

Looking at the interval with reasonably small and acceptable error ($\epsilon \leq 0.2$), there are only 27 experimental cases in that interval. The total number of experiments is 72; thus, the experimental cases with an error less than 0.2 are only 37.5%. Hence, the model does not describe the experimental data very well using an entrainment coefficient of 0.0535, which is a standard value for jets.

Figure 37 shows the relationship between the densimetric Froude number and the error calculated with equation (56). The correlation coefficient when a trend line is fitted is 0.47. This coefficient is too small to develop any relationship between the error and the Froude number in order to establish whether there is any range of Froude numbers where the error is larger. It is possible to identify large errors for any range of Froude numbers.

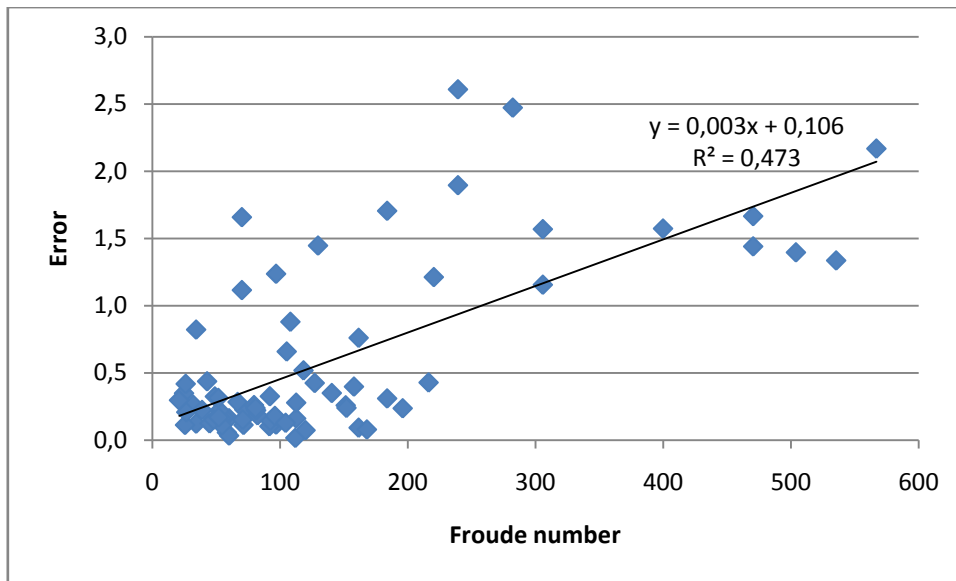


Figure 37 Simulation error versus Froude number

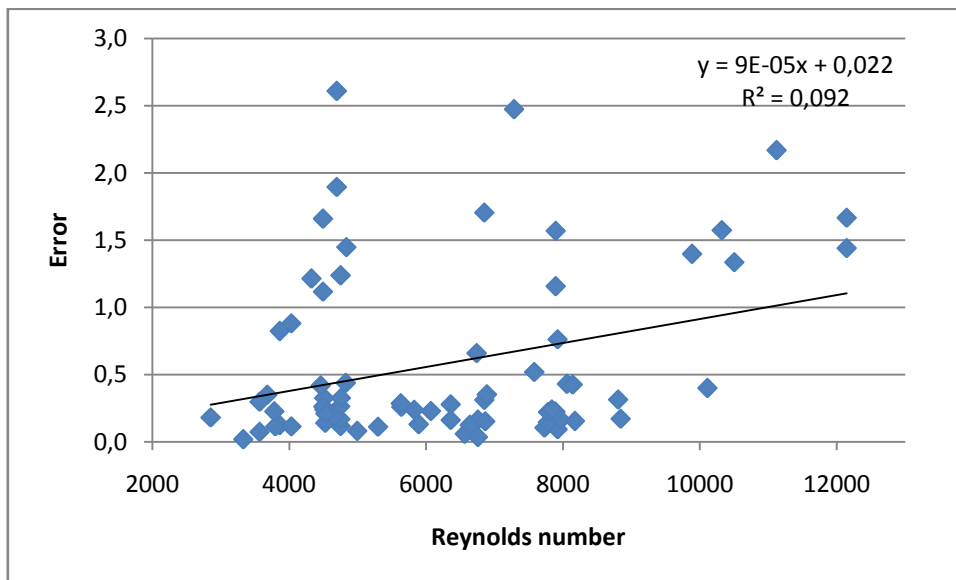


Figure 38 Simulation versus Reynolds number

Figure 38 illustrates the simulation error calculated with equation (56) as a function of the Reynolds number. The correlation coefficient is less than for the densimetric Froude number. Thus, it is possible to find large error in every range of the Reynolds number.

7.1.2 Jet trajectory comparison for calibrated entrainment coefficient

A new set of model simulations was performed in order to reduce the error between the experimental data and the model results. In these new model simulations the value on the entrainment coefficient was varied to obtain the minimum error possible for a particular experimental run.

In general, the entrainment coefficient attains different values depending on if it is a jet or a plume entraining ambient water. For a jet the standard value is 0.0535 and it can vary ± 0.0025 . In case of a plume the entrainment coefficient is 0.0833 and the variability is ± 0.0042 . A wider range of entrainment coefficient values was allowed in the present simulations and optimum coefficient values were sought in the interval 0.01 to 0.15.

Figure 39 shows the distribution of errors when the entrainment coefficient was calibrated for each experimental run. As can be observed in the figure, the error decreased significantly and 75% of the experimental runs had an error less than 0.1 and 50 experiments (69%) had an error less than 0.2.

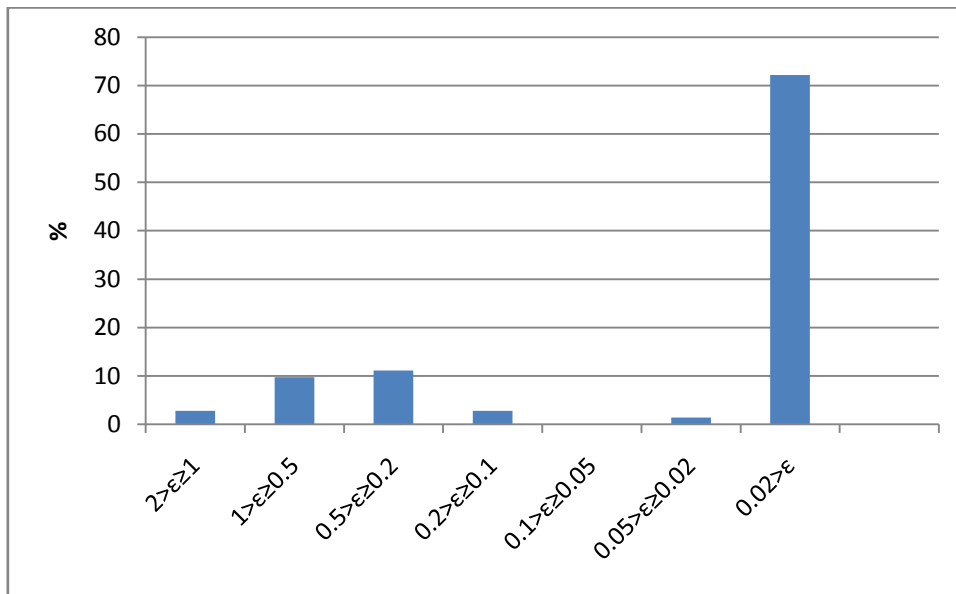


Figure 39 Distribution of simulation errors when the entrainment coefficient value was calibrated

Figure 40 shows the distribution of the entrainment coefficient when it was calibrated to minimize the error. There are a large number of runs for which the entrainment coefficient become larger than 0.1. The experimental runs yielding such values encompassed about 36% of the total number of runs. Also, it is possible to find a large number of experimental cases with low entrainment coefficient values, corresponding to almost 39% of the runs performed. Thus, only approximately 25% of the experimental cases had entrainment coefficient values in the expected range.

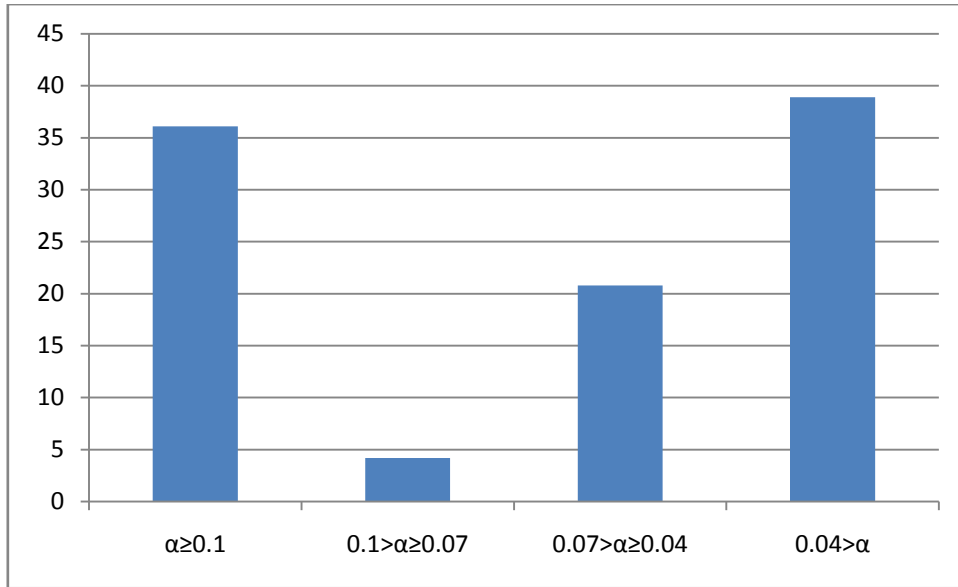


Figure 40 Distribution of the entrainment coefficient when it was calibrated against data

Figure 41 shows the distribution of entrainment coefficient with regard to the salinity employed in the experimental run. When the salinity is 2%, the entrainment coefficient obtained in the calibrations is more dispersed than for 4% or 6%. However, when the salinity is 4% there are several values corresponding to the maximum value on the entrainment coefficient permitted. These larger values occurred when the nozzle diameter was small. For the others values of 4% and when the salinity was 6% the calibrated entrainment coefficient values were in the permitted interval.

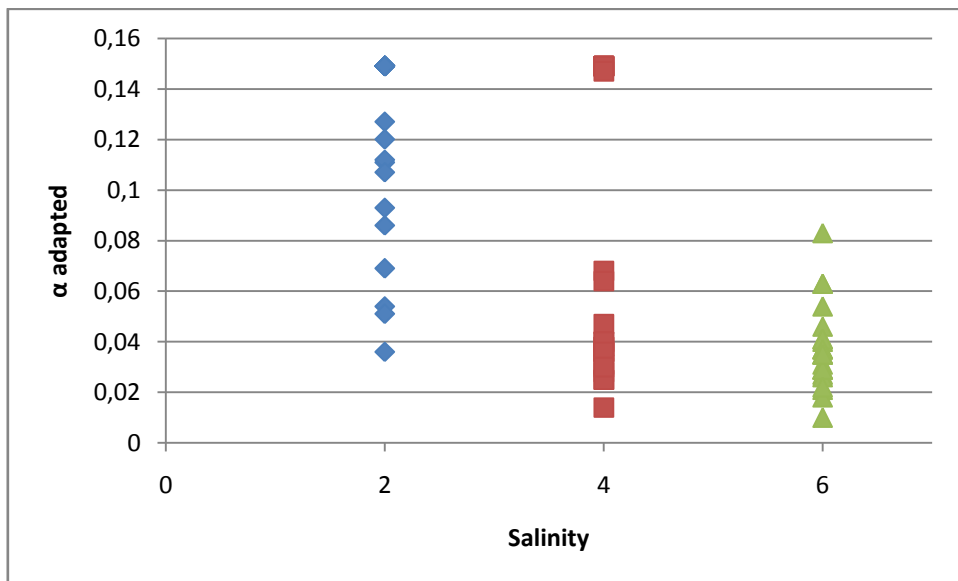


Figure 41 Distribution of the entrainment coefficient when it was calibrated against data differentiated with respect to salinity employed during the experimental run

The correlation between the calibrated entrainment coefficient values and the corresponding Froude numbers was investigated, but overall a significant scatter was observed. The calibrated entrainment coefficient values were large for some experimental runs where the Froude number was small. Thus, it was decided to focus the analysis on the runs for which the entrainment coefficient values were smaller than 0.15. Basically, a value of 0.15 implies that the model could not provide a good fit towards the data with a reasonable value on the entrainment coefficient.

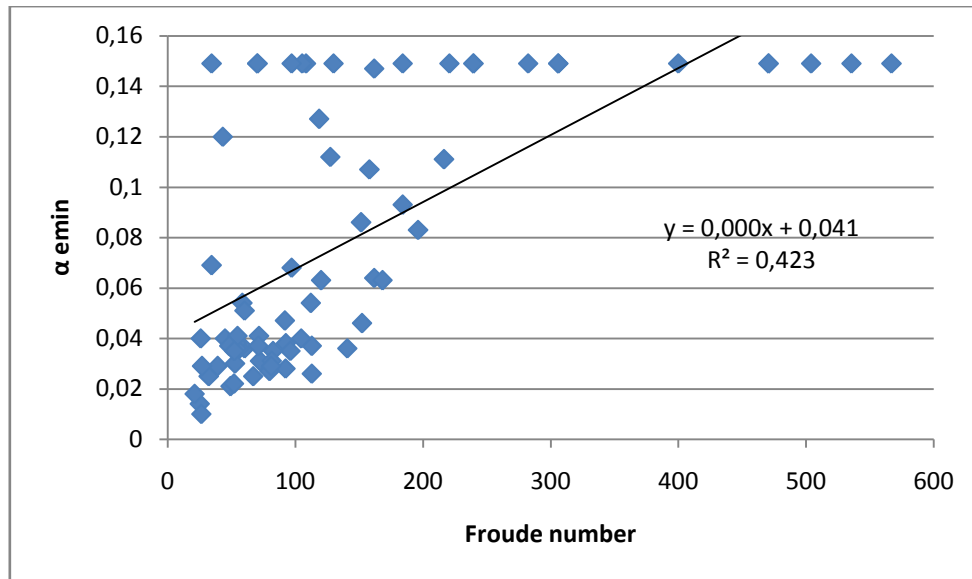


Figure 42 The entrainment coefficient when it was calibrated against data versus the densimetric Froude number

Reducing the data set, it was possible to observe a trend in the data, but the correlation coefficient for this new data set was still rather limited.

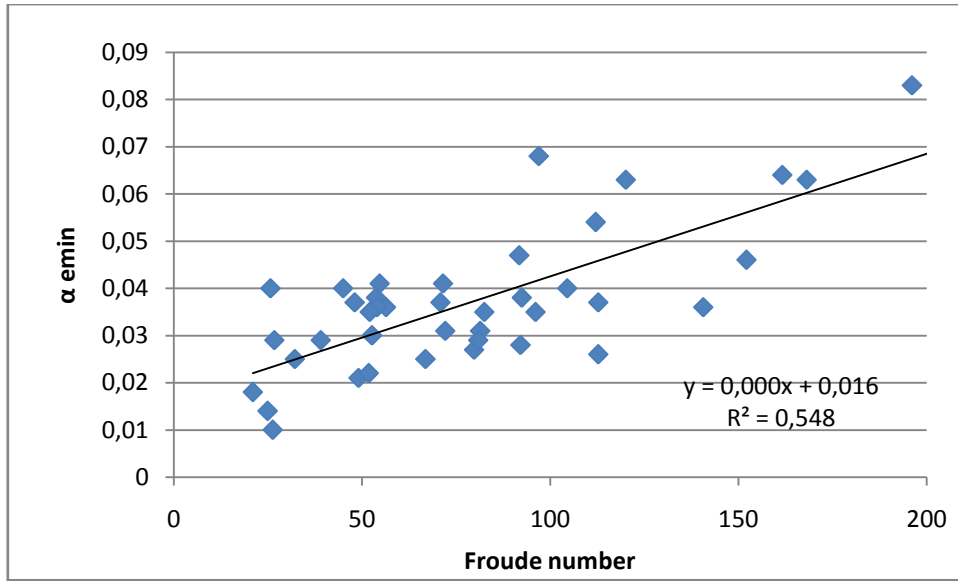


Figure 43 The entrainment coefficient when it was calibrated against data versus the densimetric Froude number for a sub-set of the data

7.2 Comparison between model simulations and data from Cipollina

Data obtained from Cipollina *et al.* (2005) were compared with the model developed in this study. The results for the Cipollina *et al.* (2005) data are better than for the present data using an entrainment coefficient with a value of 0.0535, and almost all data have an error less than 0.5. Only 9% of the data have an error larger than 0.5, and 27.3% of the data have an error less than 0.2. Figure 44 shows the distribution of the simulation error for the Cipollina *et al.* (2005) data.

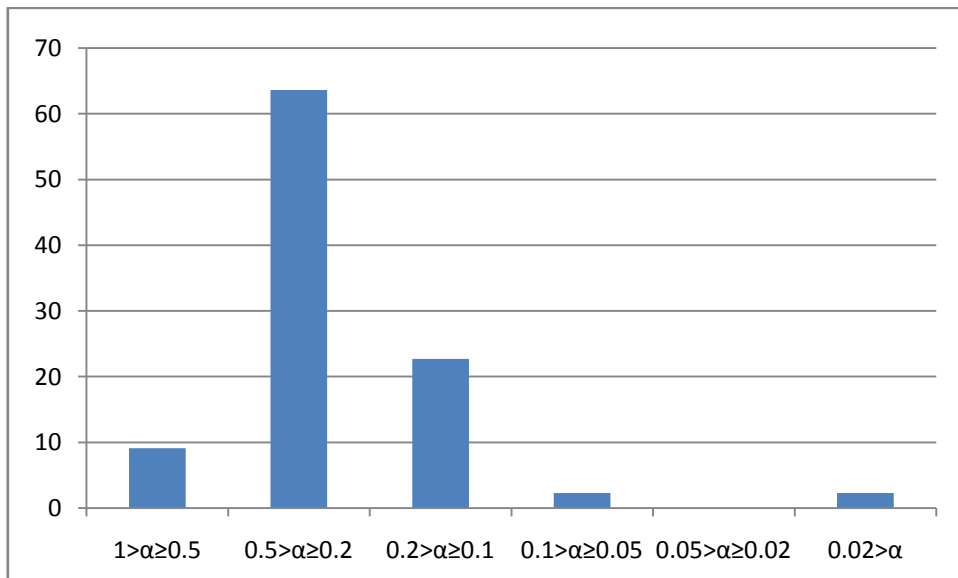


Figure 44 Distribution of simulation errors for the Cipollina *et al.* data

8. Conclusions

In the model simulations performed in this study to reproduce the experimental runs it was difficult to observe a close relationship between the model and the experimental data. For certain parameter ranges (*i.e.*, salinity, nozzle angle, nozzle diameter), model predictions were satisfactory. However, looking at different ranges in the densimetric Froude number there were always some runs that displayed larger discrepancies between the model simulations and the data obtained in the experiment. The average error was almost 0.4 and only about 37% of the 72 experimental runs had an error less than 0.2, which is judged to be an acceptable level.

When the entrainment coefficient was calibrated towards the data for each experimental run, trying to find a value that yielded the smallest difference between the model simulations and the data, the results were significantly improved (78% of experiments had an error less than 0.2), but 35% of the experimental runs still had an optimum entrainment coefficient value larger than the limiting value set in the optimization procedure (0.15), which is not physically reasonable.

When data from another experiment by Cipollina *et al.* (2005) were used to compare with model simulation results (using standard value on the entrainment coefficient), better agreement was obtained with smaller overall errors, but really good agreement was still only achieved for a limited amount of the data; only 27% of the data employed had an error less than 0.2.

A main conclusion of this study is that one or several of the assumptions used to derive the mathematical model is not satisfied in the experiment and some modifications of the equations derived are needed. Most likely a modified description of the entrainment coefficient is required that introduces a dependence on salinity and other parameters.

References

1. United States Geological Survey. (updated 09 October 2009) Available at: <http://ga.water.usgs.gov/edu/waterdistribution.html>
2. “IDA’s Desalination Yearbook 2008-2009”. Global Water Intelligence
3. Torres Corral, Miguel (2004).”Avances técnicos en la desalación de aguas”. Ambienta, Octubre 2004
4. Gleich, Peter H. (2000). “The world’s water 2000-2001”. Island press
5. US Energy Information Administration. Available at: <http://tonto.eia.doe.gov/country/index.cfm>
6. Bleninger, T., Jirka G.H. (2008). ” Modelling and environmentally sound management of brine discharges from desalination plants”. Desalination 221 (2008) 585-597
7. Ruiz Mateo, A., Antequera, M., González, F.J. (2008).” Physical modeling of brine discharges to the sea”. 5th International Conference on Marine Waste Water Discharges and Coastal Environment.
9. Zeitoun, M. A., Raid, R. O., McHillenny, W. F., and Mitchell, T. M. (1972). “Model studies of outfall systems for desalination plants. Part III. Numerical simulations and design considerations.” Res. And Devel. Progress Rep. No. 804, Office of Saline Water, U.S. Dept. of Interior, Washington, D.C.
10. Roberts, P. J. W., Ferrier, A., and Daviero, G. (1997). “Mixing in inclined dense jets.” J. Hydr. Engrg., ASCE, 123(8), 693–699.
11. Pincince, A. B., and List, E. J. (1973). “Disposal of brine into an estuary.” J. Water Pollut. Control Fed., 45, 2335–2344.
12. Jönsson, L. (2004). “Receiving Water Hydraulics”, Water Resourcesd Engineering, Lund University.
13. Cipollina A., Brucato A., Grisafi F. and Nicosia S. (2005). “Bench-Scale Investigation of Inclined Dense Jets.” J. of Hydraulic Engineering, (ASCE) 131 (11), 1017–1022.

Appendix

Table 8 Data from the laboratory experiment, where θ is the initial nozzle angle, C is the concentration, D is the diameter, Q is the flow, and x_m and y_m coordinates for the maximum centerline height and location, respectively (see Figure 30).

θ	C (%)	D (m)	Q (l/min)	$x_{m,exp}$	$y_{m,exp}$	$x_{m,mod}$	$y_{m,mod}$	ϵ
60	2	0.0015	0.38	11.5	15	44.99	49.55	2.61
60	2	0.0015	0.9	34	37.5	107.5	118.99	2.17
45	2	0.0015	0.38	17	14	55.16	35.64	1.90
45	2	0.0015	0.8	46.5	33.5	117.21	76.09	1.40
30	2	0.0015	0.35	23	8.5	50.4	18.98	1.21
30	2	0.0015	0.85	50	21.5	124.11	47.07	1.34
60	2	0.0023	0.5	16.5	17.5	30.59	33.36	0.88
60	2	0.0023	0.7	34.5	37.5	43.25	47.41	0.26
45	2	0.0023	0.6	20	11	45.19	28.97	1.45
45	2	0.0023	0.85	49	32	64.64	41.64	0.31
30	2	0.0023	0.85	23.5	9	64.17	24.11	1.70
30	2	0.0023	1	53	20	75.81	28.55	0.43
60	2	0.0033	0.8	14	13.5	27.94	30.18	1.12
60	2	0.0033	1.35	34	32.5	48.2	52.65	0.52
45	2	0.0033	0.8	13	8	34.08	21.55	1.66
45	2	0.0033	1.45	42.5	30	63.49	40.69	0.43
30	2	0.0033	1.2	26.5	14	51.6	19.19	0.66
30	2	0.0033	1.8	48	25.5	78.69	29.5	0.40
60	2	0.0048	1.25	17.5	17	24.03	25.54	0.44
60	2	0.0048	1.7	35.5	34	33.47	35.97	0.06
45	2	0.0048	1	12	8	22.75	13.98	0.82
45	2	0.0048	1.75	41.5	28	42.06	26.47	0.03

30	2	0.0048	1	18	8	22.11	7.87	0.12
30	2	0.0048	1.75	47	19	41.33	15.11	0.16
60	4	0.0015	0.6	15.5	15	50.31	55.46	2.47
60	4	0.0015	0.85	28.5	30	71.56	79.07	1.57
45	4	0.0015	0.65	24.5	18	66.92	43.3	1.57
45	4	0.0015	1	37	26.5	103.49	67.14	1.67
30	4	0.0015	0.65	28	13	66.56	25.14	1.16
30	4	0.0015	1	38	18	103.05	39.04	1.44
60	4	0.0023	0.6	19	9	25.79	28.04	1.24
60	4	0.0023	1	50	20	43.7	47.91	0.76
45	4	0.0023	0.6	30	17	31.52	20.07	0.12
45	4	0.0023	1	51.5	30	53.52	34.4	0.09
30	4	0.0023	0.57	27.5	26	29.48	10.91	0.33
30	4	0.0023	0.87	39	36	45.94	17.17	0.35
60	4	0.0033	0.86	26	26	20.87	22.36	0.17
60	4	0.0033	1.1	35	38	27.12	29.28	0.23
45	4	0.0033	0.82	29	17	24.12	15.09	0.14
45	4	0.0033	1.4	51	26	42.67	27.14	0.10
30	4	0.0033	1.02	41.5	15.5	30.01	10.99	0.28
30	4	0.0033	1.41	48	19	42.44	15.71	0.14
60	4	0.0048	1	14.5	14.5	12.65	13.06	0.11
60	4	0.0048	1.75	27	29	23.76	25.24	0.12
45	4	0.0048	1.25	27.5	16	19.77	12.07	0.26
45	4	0.0048	2.1	44.5	25	35.23	22.04	0.16
30	4	0.0048	0.97	19.5	8.5	14.14	4.9	0.35
30	4	0.0048	2.05	39	17.5	33.61	12.2	0.22
60	6	0.0015	0.28	19	20	18.74	20.41	0.02

60	6	0.0015	0.49	27	29.5	33.31	36.59	0.24
45	6	0.0015	0.24	24	15	19.5	12.4	0.18
45	6	0.0015	0.38	27	29.5	31.43	20.17	0.24
30	6	0.0015	0.3	24	8	24.35	9.06	0.07
30	6	0.0015	0.42	32	12	34.56	12.95	0.08
60	6	0.0023	0.6	28	25.5	20.86	22.58	0.18
60	6	0.0023	0.82	36	36	28.9	31.49	0.16
45	6	0.0023	0.52	24	16	21.87	13.8	0.11
45	6	0.0023	0.76	41	22	32.65	20.8	0.13
30	6	0.0023	0.58	28	14.5	24.2	8.91	0.26
30	6	0.0023	0.82	41	22	34.94	12.99	0.28
60	6	0.0033	0.7	18.5	17	13.37	14.08	0.22
60	6	0.0033	1.27	31.5	31	25.48	27.46	0.15
45	6	0.0033	0.98	25	17.5	23.49	14.68	0.11
45	6	0.0033	1.46	46	29.5	36.02	22.81	0.22
30	6	0.0033	0.88	30	11	20.41	7.37	0.32
30	6	0.0033	1.45	44	18	35.23	12.97	0.24
60	6	0.0048	1.22	15	17.5	12.6	13	0.21
60	6	0.0048	2.2	27	33	24.45	26	0.15
45	6	0.0048	0.96	15.5	10	11.36	6.72	0.30
45	6	0.0048	2.38	38	25	32.37	20.19	0.17
30	6	0.0048	1.2	21.5	10	14.32	4.97	0.42
30	6	0.0048	2.37	45	17	31.53	11.41	0.31

Table 9 Errors between experimental runs and the model simulation, calibrating the entrainment coefficient to obtain minimum difference.

θ	C (%)	D (m)	Q (l/min)	α	ε
60	2	0.0015	0.38	0.149	1.18
60	2	0.0015	0.9	0.149	0.91
45	2	0.0015	0.38	0.149	0.75
45	2	0.0015	0.8	0.149	0.44
30	2	0.0015	0.35	0.149	0.34
30	2	0.0015	0.85	0.149	0.41
60	2	0.0023	0.5	0.149	0.15
60	2	0.0023	0.7	0.086	0.00
45	2	0.0023	0.6	0.149	0.49
45	2	0.0023	0.85	0.093	0.00
30	2	0.0023	0.85	0.149	0.65
30	2	0.0023	1	0.111	0.00
60	2	0.0033	0.8	0.149	0.31
60	2	0.0033	1.35	0.127	0.00
45	2	0.0033	0.8	0.149	0.65
45	2	0.0033	1.45	0.112	0.00
30	2	0.0033	1.2	0.149	0.02
30	2	0.0033	1.8	0.107	0.00
60	2	0.0048	1.25	0.12	0.00
60	2	0.0048	1.7	0.054	0.00
45	2	0.0048	1	0.149	0.16
45	2	0.0048	1.75	0.051	0.00
30	2	0.0048	1	0.069	0.00
30	2	0.0048	1.75	0.036	0.00
60	4	0.0015	0.6	0.149	1.10

60	4	0.0015	0.85	0.149	0.55
45	4	0.0015	0.65	0.149	0.55
45	4	0.0015	1	0.149	0.61
30	4	0.0015	0.65	0.149	0.30
30	4	0.0015	1	0.149	0.47
60	4	0.0023	0.6	0.149	0.37
60	4	0.0023	1	0.147	0.00
45	4	0.0023	0.6	0.068	0.00
45	4	0.0023	1	0.064	0.00
30	4	0.0023	0.57	0.028	0.01
30	4	0.0023	0.87	0.036	0.00
60	4	0.0033	0.86	0.036	-0.01
60	4	0.0033	1.1	0.031	-0.01
45	4	0.0033	0.82	0.038	0.00
45	4	0.0033	1.4	0.047	0.00
30	4	0.0033	1.02	0.025	0.00
30	4	0.0033	1.41	0.038	0.00
60	4	0.0048	1	0.04	0.00
60	4	0.0048	1.75	0.04	0.00
45	4	0.0048	1.25	0.025	-0.01
45	4	0.0048	2.1	0.036	0.00
30	4	0.0048	0.97	0.014	0.01
30	4	0.0048	2.05	0.03	0.00
60	6	0.0015	0.28	0.054	0.00
60	6	0.0015	0.49	0.083	0.00
45	6	0.0015	0.24	0.035	0.00
45	6	0.0015	0.38	0.046	-0.01

30	6	0.0015	0.3	0.063	0.00
30	6	0.0015	0.42	0.063	0.00
60	6	0.0023	0.6	0.035	-0.01
60	6	0.0023	0.82	0.037	0.00
45	6	0.0023	0.52	0.041	0.00
45	6	0.0023	0.76	0.04	0.00
30	6	0.0023	0.58	0.027	0.01
30	6	0.0023	0.82	0.026	0.01
60	6	0.0033	0.7	0.029	0.00
60	6	0.0033	1.27	0.037	0.00
45	6	0.0033	0.98	0.041	0.00
45	6	0.0033	1.46	0.031	0.00
30	6	0.0033	0.88	0.021	-0.01
30	6	0.0033	1.45	0.029	0.00
60	6	0.0048	1.22	0.029	0.00
60	6	0.0048	2.2	0.037	0.00
45	6	0.0048	0.96	0.018	0.00
45	6	0.0048	2.38	0.035	0.00
30	6	0.0048	1.2	0.01	-0.01
30	6	0.0048	2.37	0.022	-0.01